

Flow Regimes over a Basin Induced by Upstream Katabatic Flows—An Idealized Modeling Study

MANUELA LEHNER

Department of Atmospheric Sciences, University of Utah, Salt Lake City, Utah

RICHARD ROTUNNO

National Center for Atmospheric Research, Boulder, Colorado

C. DAVID WHITEMAN

Department of Atmospheric Sciences, University of Utah, Salt Lake City, Utah

(Manuscript received 12 April 2016, in final form 14 June 2016)

ABSTRACT

Idealized two-dimensional model simulations are performed to study the frequent nocturnal occurrence of downslope-windstorm-type flows in Arizona's Meteor Crater. The model topography is a simplified representation of the Meteor Crater and its surroundings, with an approximately 1° mesoscale slope upstream and downstream of the crater basin. A strong surface-based inversion and a katabatic flow develop above the mesoscale slope as a result of radiational cooling. The temperature and flow profiles are evaluated against observations over low-angle slopes from two field campaigns, showing that the model's turbulence parameterization has a strong impact on the near-surface conditions. The interaction of the katabatic flow with the basin topography leads to the formation of waves and hydraulic jumps over the basin. The simplified two-dimensional simulations show good qualitative agreement with observations of downslope-windstorm-type flows from the Meteor Crater. The sensitivity of the flow solution over the basin to basin depth, basin width, and background wind speed is investigated. The resulting flow regimes include a sweeping of the basin atmosphere, a wake over the upstream crater sidewall, waves over the basin with one or two wave crests, and a hydraulic jump. The regimes are discussed in the context of stratified flow over mountains.

1. Introduction

Downslope windstorms occur throughout the world in the lee of large mountain ranges as synoptic winds perpendicular to the mountain flow over the barrier and descend and accelerate in the lee, where the resulting wind speeds can reach damaging magnitudes. Downslope windstorms have been studied in many high-mountain locations, including the Wasatch Mountains in Utah (Lawson and Horel 2015), the Sierra Nevada (Mayr and Armi 2010), the European Alps (Richner and Hächler 2012), the Adriatic coastal mountains (Grisogono and Belušić 2009), and the Andes (Seluchi et al. 2003).

Lawson and Horel (2015) report wind gusts of up to 45 m s^{-1} along the Wasatch Front in Utah during a December 2011 downslope windstorm. During the 11 January 1972 windstorm in Boulder, Colorado, wind gusts of over 50 m s^{-1} were recorded (Lilly 1978). Downslope windstorms have not only been observed in the lee of large mountain ranges, but also in the lee of smaller mountains, for example, the Falkland Islands (Mobbs et al. 2005).

At Arizona's Meteor Crater, nocturnal downslope windstorms occur frequently on the inner southwest crater sidewall driven by a katabatic flow that forms upstream of the crater (Adler et al. 2012; Lehner et al. 2016). An example of the flow over the crater is shown in Fig. 1. The approximately 1200-m-wide (approximately 500-m-wide basin floor) and 170-m-deep Meteor Crater is located on a mesoscale plain that slopes slightly down to the northeast. During quiescent, clear-sky nights a

Corresponding author address: Manuela Lehner, Institute of Atmospheric and Cryospheric Sciences, University of Innsbruck, Innrain 52f, A-6020 Innsbruck, Austria.
E-mail: manuela.lehner@uibk.ac.at

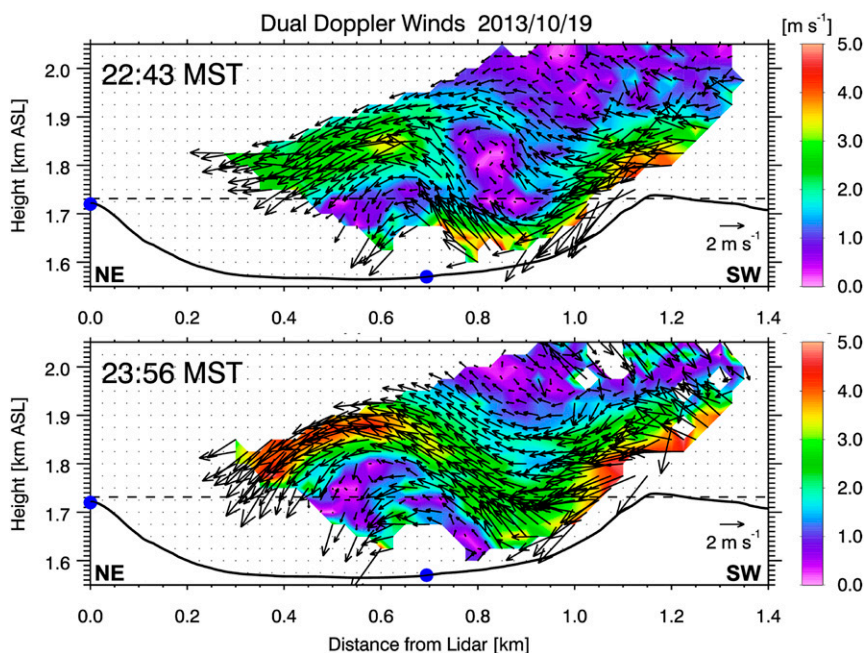


FIG. 1. Wind speed and wind arrows in a northeast–southwest cross section through the Meteor Crater from a dual Doppler lidar analysis during METCRAX II, (top) 2243 and (bottom) 2356 MST 19 Oct 2013. The blue dots show the locations of the two scanning lidars.

southwesterly drainage flow forms over the plain, which impinges on the approximately 30–50-m-high crater rim. Under favorable conditions the flow over the crater leads to the formation of a deep wave in the lee of the upwind rim and downslope-windstorm-type flows on the crater’s southwest inner sidewall. During these events, strong and gusty winds are observed along the sidewall, and temperatures over the southwest sidewall can be up to 7°C higher than over the crater center. The second Meteor Crater experiment (METCRAX II) took place in October 2013 to study the downslope-windstorm-type flows in the Meteor Crater and the conditions that lead to their formation (Lehner et al. 2016).

Stratified flows over mountains have been studied extensively, and overviews of the theory and results from observations and numerical simulations can be found, for example, in Baines (1995), Durran (2003a,b), and Jackson et al. (2012). Comparatively little is known about stratified flows over depressions, such as valleys or basins. The response to flow over mountains is often-times characterized by nondimensional numbers, such as the nondimensional mountain height $\hat{H} = NH/U$ (Jackson et al. 2012), where $N = \sqrt{(g/\theta)(d\theta/dz)}$ is the Brunt–Väisälä frequency, H is the mountain height, U is the upstream wind speed perpendicular to the obstacle, g is acceleration due to gravity, and θ is potential temperature. The nondimensional mountain height \hat{H} indicates whether the flow approaching a mountain

barrier has sufficient inertia to go over the mountain ($\hat{H} \leq 1$) or whether it becomes blocked on the upstream side or has to flow around the mountain. It is also called the nonlinearity parameter because it also indicates whether nonlinear processes are important ($\hat{H} > 1$). The inverse of \hat{H} is often termed a Froude number (Baines 1995). As the stability and wind speed typically vary with height and location, the actual calculation of these nondimensional numbers differs from study to study (e.g., Kimura and Manins 1988). Analogous to \hat{H} , a nondimensional valley or basin depth $\hat{D} = ND/U$ can be defined, where D is the valley or basin depth (Vosper and Brown 2008). Several studies have shown that \hat{D} is a measure of flow decoupling over the valley atmosphere (e.g., Holden et al. 2000; Vosper and Brown 2008; Sheridan et al. 2014).

The majority of studies looking at flow over valleys under stable conditions have focused on the erosion of cold-air pools (e.g., Lareau and Horel 2015) and the conditions in which the valley atmosphere stagnates and decouples from the atmosphere aloft or in which a sweeping of the valley atmosphere occurs. Sheridan et al. (2014) used the nondimensional valley depth to forecast the cold-air pool strength in two small valleys in the United Kingdom and found a critical value for decoupling of the valley atmosphere of $\hat{D} \approx 1$. Below the critical value, the cold-air pool strength increases with increasing \hat{D} , whereas it becomes independent of \hat{D}

above the critical value. [Smith et al. \(2010\)](#) found a critical value of $\hat{D} = 0.1$ – 1 based on numerical simulations for a region over southwest England, while [LeMone et al. \(2003\)](#) determined a value of $\hat{D} \approx 1/3$ for a shallow watershed in Kansas, and [Holden et al. \(2000\)](#) found a critical value of $\hat{D} \approx 0.5$ based on tethered observations in a valley in Wales. Idealized two-dimensional simulations of flow over a valley by [Vosper and Brown \(2008\)](#) showed critical \hat{D} values for decoupling of 0.35 – 0.64 . [Holden et al. \(2000\)](#) suggest four possible responses to flow over a valley: (i) attached flow that follows the underlying surface and ventilates the valley, (ii) attached flow with a phase shift with height, (iii) flow separation on the upstream sidewall, and (iv) decoupling from the atmosphere aloft and stagnation of the valley atmosphere. They suggest that (i) and (iii) can occur under neutral conditions. They also mention that stable conditions have received less attention than neutral conditions. Numerical simulations of stratified flow over a series of ridges and valleys by [Kimura and Manins \(1988\)](#) found cases of sweeping, blocking, wave breaking, and partial blocking for inviscid cases and sweeping, complete stagnation, and rotor formation for dissipative cases. [Vosper and Brown \(2008\)](#) also found waves over a valley depending on atmospheric stratification.

A topographic setting that has similarities to depressions and that has been studied with respect to the formation of waves is the double-mountain system: that is, a valley between two mountains. An example of such a double-mountain system is the Owens Valley in California. Removing the downstream mountains in numerical simulations shows that their existence leads to interference effects that impact gravity waves over the Owens Valley ([Grubišić and Billings 2007](#)). [Grubišić and Stiperski \(2009\)](#) performed idealized simulations to study the effect of a second obstacle downstream of a mountain on the gravity waves behind the first obstacle and found that the presence of the second mountain affects the amount of wave trapping, the wavelength, and the number of wave crests across the valley.

The goal of the present study is to gain an understanding of flow regimes over basins and the impact of basin size and upstream flow and temperature profiles using idealized two-dimensional numerical model simulations. The findings are applied to explain the observed downslope-windstorm-type flows at the Meteor Crater in the context of the crater's size and upstream flow conditions. Numerical simulations of flow over craters have been performed for small idealized craters of the size of the Meteor Crater ([Fritts et al. 2010](#); [Kiefer and Zhong 2011](#); [Katurji et al. 2013](#)), including Martian craters ([Rafkin et al. 2001](#)), as well as for large 100-km-wide craters ([Soontiens et al. 2013](#)). With the exception of

[Kiefer and Zhong \(2011\)](#), however, the above studies prescribed a wind field to force the flow over the crater. [Kiefer and Zhong \(2011\)](#) studied cold-air intrusions into the Meteor Crater, which occur as cold air accumulates upstream of the southwest crater rim and eventually drains into the crater, producing a distinctive three-layer temperature structure ([Whiteman et al. 2010](#); [Haiden et al. 2011](#)). They ran two-dimensional simulations with a mesoscale slope upstream of the crater, where katabatic flows formed naturally in the model, producing the cold-air inflow into the crater. Our setup is similar to the one by [Kiefer and Zhong \(2011\)](#) in that the flow over the basin is produced through radiative cooling over the sloping plain upstream of the basin.

The model and the simulation design are described in [section 2](#). In [section 3](#), a comparison of the modeled upstream conditions with observations from METCRAX II and from the Vertical Transport and Mixing Experiment (VTMX; [Doran et al. 2002](#)) is given. The two-dimensional model simulations of flow over a basin are presented in [section 4](#). In [section 5](#), the results are further discussed, and conclusions are given in [section 6](#).

2. Model description and setup

Two-dimensional model simulations are run with the Cloud Model 1 (CM1) release 17 ([Bryan and Fritsch 2002](#)). The model topography is an idealized representation of a cross section through the Meteor Crater and its surrounding plain ([Fig. 2](#)). It consists of a two-dimensional slope with a slope angle of 1° , which corresponds to an approximate elevation gain of 600 m over a horizontal distance of 35 km. A basin with a flat basin floor is inserted in the center of the slope. Two 5-km-wide flat plateaus are located at each end of the approximately 35-km-long slope to reduce errors at the streamwise domain boundaries, where open boundary conditions are applied. In the cross-slope direction, three grid points are used with periodic boundary conditions. As mentioned by [Soontiens et al. \(2013\)](#), the topography of craters and basins is inherently three-dimensional, leading to effects such as flow splitting or flow convergence in the basin. From METCRAX II observations it is known that three-dimensional effects do indeed affect the flow in and over the crater. In this study, however, we will show that the flow can be reproduced qualitatively by two-dimensional simulations. The computational efficiency and the relative simplicity of the two-dimensional simulations facilitate the analysis of the physics driving the downslope-windstorm-type flows at the Meteor Crater and the analysis of a larger parameter space. The impact of three-dimensional effects is left for future work.

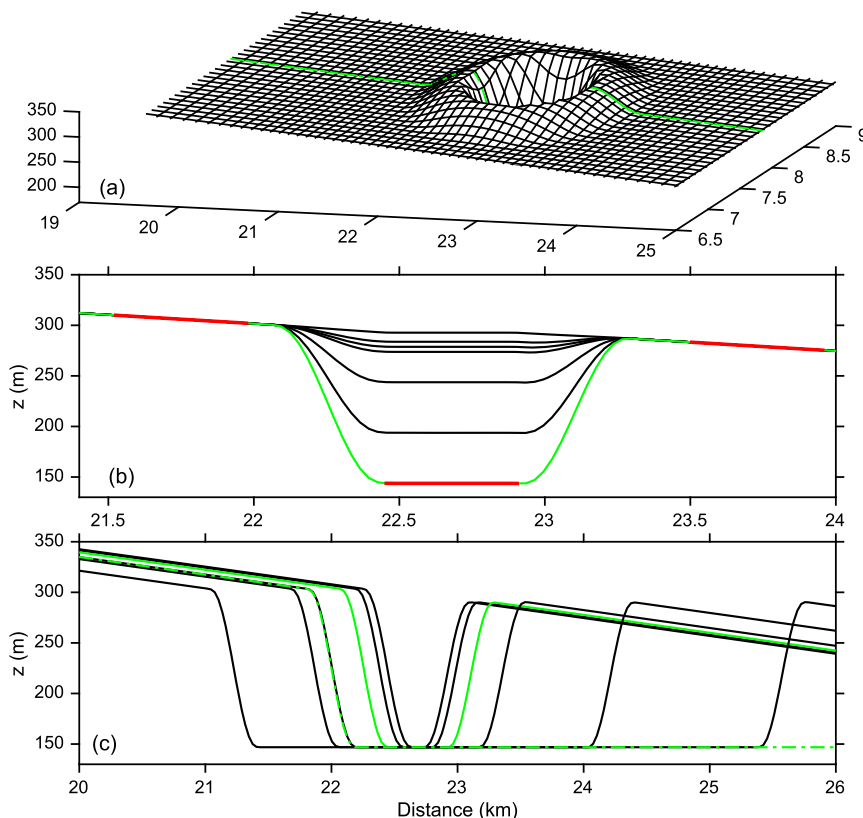


FIG. 2. (a) Center section of the model topography (m) for 3D simulations (19–25 km \times 6.5–9 km); (b) 2D model topographies for basin depths of 5, 10, 15, 20, 50, 100, and 150 m and a basin floor width of 500 m; and (c) 2D model topographies for basin widths of 125, 250, 500, 1000, 2000, 4000, and ∞ m and a basin depth of 150 m. The green line in (a) indicates the cross section used for the 2D topographies but without the rim. The model topography with dimensions similar to the Meteor Crater is shown by the solid green line in (b) and (c). The dashed green line in (c) shows the topography for the infinitely wide basin, and the red lines in (b) highlight the areas used for the calculation of the heat deficit and vertically integrated momentum in Fig. 11.

To test the sensitivity of the flow response to basin size, simulations are run with basin depths of 5–150 m and basin-floor widths of 125 m to 4 km, as well as a semi-infinitely wide basin, for which the topography downstream of the upstream basin sidewall is replaced with flat terrain. The basin that corresponds most closely to the Meteor Crater is 150 m deep with a 500-m-wide basin floor. While the Meteor Crater is surrounded by a 30–50-m-high rim, no rim is used in these simulations to avoid blocking effects, which may affect the upstream flow conditions.

The grid is stretched in the streamwise direction, with a 30-m grid spacing in the center over the crater and its nearby surroundings, which is stretched to 150 m at the domain boundaries. The length of the 30-m section depends on the basin width. A constant grid spacing of 30 m is used in the cross-slope direction. The simulated katabatic flow is evaluated against observations in section 3, showing that the 30-m grid spacing gives

reasonable results. However, to test the sensitivity of the results to horizontal resolution, some of the simulations were rerun with a 10-m grid spacing in the center (not shown). The higher resolution affected the katabatic-wind speed and thus the flow response over the basin, but to a smaller degree than certain changes in the turbulence parameterization described in section 3. In the vertical direction, the grid spacing is stretched from 2 m within the lowest 30 m above the surface to 150 m above approximately 3000 m. The total atmosphere is about 6 km deep, with a Rayleigh damping layer above 4 km.

The simulations are initialized with a dry (1% relative humidity) atmosphere and a horizontally homogeneous temperature field with a vertical potential temperature gradient of 0.5 K km^{-1} . The first set of simulations (experiment EXPDEP; Table 1) is initialized with 0 m s^{-1} wind speeds so that the flow over the basin is entirely due to the mesoscale katabatic flow. To test the sensitivity of the results to the wind speed, additional

TABLE 1. Summary of model simulations: width of the basin floor W , basin depths D , and initial wind speed u_{00} used in combination with the respective basin-floor width, experiment name, and the section that discusses results from the respective experiment.

W (m)	D (m)	u_{00} (m s^{-1})	Experiment	Section
125	10, 15, 20, 50, 100, 150	0	EXPWID	4c
250	10, 15, 20, 50, 100, 150	0	EXPWID	4c
500	5, 10, 15, 20, 50, 100, 150	0	EXPDEP	4, 5
500	10, 15, 20, 50, 100, 150	2, 5, 7, 10, 15	EXPSPD	4b, 5
1000	10, 15, 20, 50, 100, 150	0	EXPWID	4c
2000	10, 15, 20, 50, 100, 150	0	EXPWID	4c
4000	10, 15, 20, 50, 100, 150	0	EXPWID	4c
∞	10, 15, 20, 50, 100, 150	0, 2, 5, 7, 10, 15	EXPWID	4c

simulations are initialized with 2, 5, 7, 10, and 15 m s^{-1} in the direction of the katabatic flow (experiment EXPSPD; Table 1). The surface layer model is the fifth-generation Pennsylvania State University–National Center for Atmospheric Research Mesoscale Model (MM5; Grell et al. 1995) surface layer model, which is based on Monin–Obukhov similarity theory and is also implemented in the Weather Research and Forecasting (WRF) Model (Skamarock et al. 2008). Initial surface temperature is extrapolated from the air temperature at the first two model levels, and a constant land-use category of barren or sparsely vegetated land is used with a surface roughness length of 0.01 m. The turbulence parameterization is discussed in section 3. No artificial diffusion is used other than the implicit diffusion arising from the fifth-order advection scheme.

The model simulations are run for a 6-h period, starting approximately 1 h after astronomic sunset at the location of the Meteor Crater (35°N, 111°W). Since the simulations start after sunset, only longwave radiation is active (NASA Goddard longwave radiation code; Chou and Suarez 1994; Tao et al. 1996). The time step is 0.1 s (with eight acoustic time steps), and model fields are averaged over 10-min periods before being output.

3. Katabatic flow

Observations from METCRAX II have shown that the depth and strength of the mesoscale drainage flow upstream of the crater are key factors in determining the formation and strength of downslope-windstorm-type flows in the Meteor Crater (Lehner et al. 2016). Reproducing a realistic drainage flow profile upstream and at the edge of the crater thus seems of paramount importance, as confirmed by initial simulations (not shown). In this section, we will therefore validate the model's ability to reproduce the upstream surface inversion and drainage flow correctly. To this purpose, a series of simulations was run with various turbulence parameterizations. The simulation setup was equivalent to the one described in section 2 but without a basin and

without initial winds. The model results were compared to observations taken during the VTMX field campaign. The VTMX field campaign took place in 2000 in the Salt Lake Valley, Utah, with a focus on vertical transport and mixing processes of heat, momentum, and air pollutants in the nocturnal atmosphere in mountainous terrain (Doran et al. 2002). During the field campaign, downslope flows were measured on a relatively homogeneous, low-angle slope on the west side of the Salt Lake Valley (Haiden and Whiteman 2005; Whiteman and Zhong 2008; Zhong and Whiteman 2008). Three tethersondes were operated concurrently along a line down the slope during eight intensive observational periods (IOPs). Katabatic flows were observed on all clear and undisturbed nights, with typical depths of 100–150 m and jet maxima of 5–6 m s^{-1} at a height of about 15 m above the ground. Strong temperature inversions were measured over the slope, with typical temperature increases of 7°C over a 25-m layer (Whiteman and Zhong 2008). The downslope flows observed during VTMX were successfully modeled by Zhong and Whiteman (2008) using a mesoscale model [Regional Atmospheric Modeling System (RAMS); Cotton et al. 2003] and a TKE-based turbulence parameterization scheme (Mellor and Yamada 1982).

As discussed in previous studies, katabatic flows can pose challenges for turbulence parameterizations. While the stability in the surface-based stable layer suppresses turbulence and thus momentum and heat fluxes, wind shear due to the characteristic jet profile produces turbulence (Horst and Doran 1988; Zardi and Whiteman 2012). At the height of the jet maximum, the wind shear and thus turbulence production reach a minimum, which means that the layer below the jet maximum and the layer above the jet maximum become decoupled (Zhong and Chow 2012). Arritt and Pielke (1986), however, noted that to simulate katabatic flows correctly turbulence transfer across the jet maximum must be possible.

The results of the model comparison with VTMX observations show that the turbulent mixing parameterization—that is, the magnitudes of the vertical eddy viscosity

TABLE 2. Summary of katabatic flow simulations with different turbulence parameterizations: parameterization identifier, definition of K_m , Prandtl number $\text{Pr} = K_m/K_h$, minimum value for K_m where applicable, and the field campaign from which data were used for model comparison. Also S is vertical wind shear, $\text{Ri} = N^2/S^2$ is the Richardson number, l_m is a vertical length scale, e is turbulent kinetic energy, and Δx , Δy , and Δz are gridpoint distances in the two horizontal and in the vertical directions.

Parameterization	K_m	Pr	K_{\min}	Field campaign
L	$l_m^2 S \sqrt{1 - \text{Ri}}$	1	—	VTMX, METCRAX II
LK _m	$l_m^2 S \sqrt{1 - \text{Ri}}$	1	$0.15 \text{ m}^2 \text{ s}^{-1}$	VTMX
B	$l_m^2 S$	1	—	VTMX, METCRAX II
BK _m	$l_m^2 S$	1	$0.15 \text{ m}^2 \text{ s}^{-1}$	VTMX
K0.15	$0.15 \text{ m}^2 \text{ s}^{-1}$	1	—	VTMX, METCRAX II
TKE	Prognostic TKE equation	1	—	VTMX
TKEK _m	Prognostic TKE equation	3 (for $N^2 \leq 0$) $1 + 2 \frac{0.8165 \sqrt{e}}{N(\Delta x \Delta y \Delta z)^{1/3}}$ (for $N^2 > 0$)	$0.15 \text{ m}^2 \text{ s}^{-1}$	VTMX, METCRAX II

K_{mv} and heat diffusivity K_{hv} —have a large impact on the near-surface temperature and wind profiles. Horizontal mixing is turned off in all simulations; that is, $K_{hh} = K_{mh} = 0 \text{ m}^2 \text{ s}^{-1}$. We will therefore neglect the subscripts v and h from here on and simply use K_m and K_h when referring to the vertical diffusion coefficients of momentum and heat, respectively. The quantities K_m and K_h are related by the Prandtl number $\text{Pr} = K_m/K_h$, which typically depends on atmospheric stability. A value of $\text{Pr} = 1$ is oftentimes assumed for very stable conditions. Cuxart and Jiménez (2007) found a value of 0.8 above the jet maximum in their simulations of low-level jets and even smaller values below the jet maximum, while Axelsen and van Dop (2009b) found that Pr depends on the gradient Richardson number Ri ($\text{Pr} = 0.5 + 4.5\text{Ri}$) in their large-eddy simulations of katabatic flows, similar to the findings by Zilitinkevich et al. (2008) ($\text{Pr} = 0.8 + 5\text{Ri}$).

Previous model simulations of downslope flows have used a wide range of different models, ranging from mesoscale models (e.g., Zhong and Whiteman 2008) to large-eddy simulations (e.g., Skillingstad 2003; Smith and Skillingstad 2005; Axelsen and van Dop 2009a,b; Grisogono and Axelsen 2012; Smith and Porté-Agel 2014) and to direct numerical simulations (Fedorovich and Shapiro 2009). Many of the simulations used a turbulent kinetic energy (TKE)-based turbulence scheme (e.g., Zhong and Whiteman 2008; Axelsen and van Dop 2009a,b), including early simulations of downslope flows (see Denby 1999). Smith and Porté-Agel (2014) compared the performance of different subgrid models for large-eddy simulations of downslope flows, a Smagorinsky model, and two dynamic models. Different turbulence parameterization schemes were also compared with results from a large-eddy simulation for stable conditions, although not katabatic flows, by Cuxart et al. (2006).

The katabatic flow simulations with different turbulence parameterizations are listed in Table 2. The 1.5-order TKE

scheme based on Deardorff (1980) and the first-order scheme L based on Louis (1979) are standard schemes built into CM1. Parameterizations of the type $K_m = l_m^2 S f(\text{Ri})$ based on Louis (1979) have been commonly used with varying stability functions $f(\text{Ri})$ in operational weather forecasting models: for example, in the ECMWF model (Louis et al. 1982; Viterbo et al. 1999; Bechtold et al. 2008) and the Met Office Unified Model (McCabe and Brown 2007; Brown et al. 2008; Lock 2011). This type of parameterization was also used for a katabatic flow model by Haiden (2003). The stability functions are traditionally based on Monin–Obukhov similarity theory or on the Richardson number (Mauritsen 2011). In the above definition of K , S is the vertical wind shear, and l_m is a vertical length scale (Mason and Brown 1999). For the simulations listed in Table 2, l_m is defined as

$$l_m = \frac{1}{\sqrt{1/l_\infty^2 + 1/(\kappa z + z_0)^2}}, \quad (1)$$

where $l_\infty = 3 \text{ m}$, $\kappa = 0.4$ is the von Kármán constant, and $z_0 = 0.01 \text{ m}$ is the surface roughness length. A relatively low value for l_∞ was required based on test simulations (not shown) to avoid unrealistic smoothing of the vertical profiles in the very stable near-surface atmosphere. In the TKE scheme, $K_m = 0.1 l_e \sqrt{e}$, where e is TKE and $l_e = 0.8165 \sqrt{e}/N$ (for $N^2 > 0$) or $l_e = (\Delta x \Delta y \Delta z)^{1/3}$ (for $N^2 \leq 0$) is a length scale. Turbulent kinetic energy e is a prognostic variable, determined by advection, shear production, buoyancy, turbulent mixing, and dissipation.

Both the TKE scheme and the first-order scheme L contain a dependency of K_m on static stability, which can result in extremely small mixing coefficients within the surface-based inversion. As a result of the reduced mixing, the simulated inversion may become too strong and the drainage flow too shallow. Zilitinkevich et al. (2007, 2008, 2009, 2013) developed an energy- and flux-budget turbulence closure model that can maintain turbulence

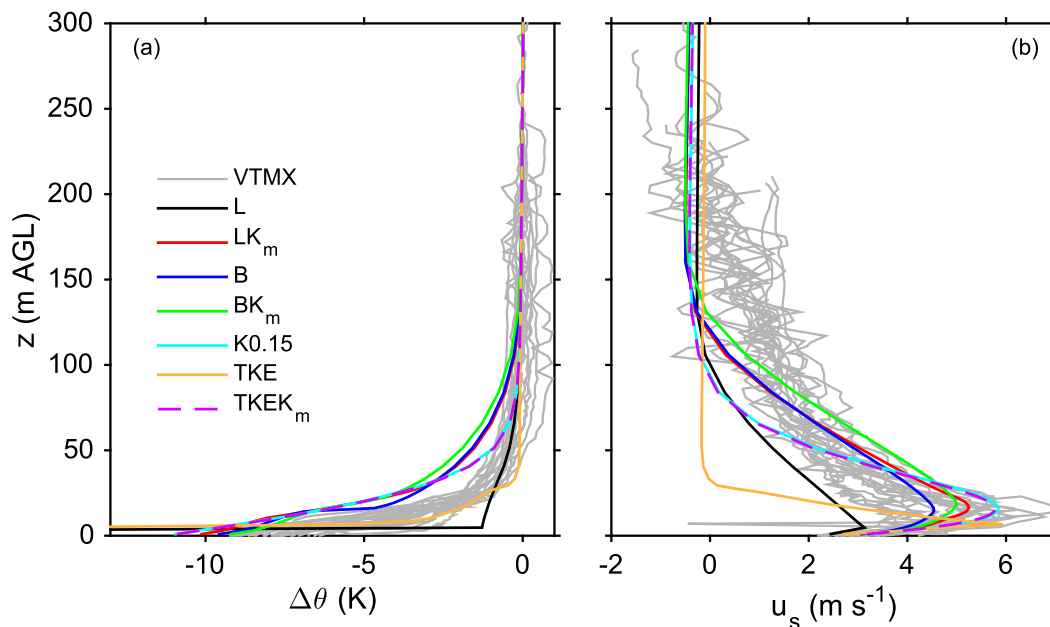


FIG. 3. Vertical profiles of (a) the potential temperature deficit and (b) the along-slope wind component from VTMX tethered-balloon soundings (light gray lines) and from the model simulations listed in Table 2 (colored lines). VTMX profiles are from 1830–2130 MST 02 Oct 2000 from three different locations along the slope, with six soundings per site (see Whiteman and Zhong 2008). The potential temperature deviation $\Delta\theta$ is the difference between potential temperature θ and potential temperature at approximately 250 m AGL or at the top of the sounding, whichever is lower.

even under very stable conditions. Here, however, the comparison is limited to a set of comparatively simpler schemes. For simulation B, the stability dependence was neglected, simplifying K_m to a function of vertical wind shear, similar to Blackadar (1962). The simulations were also repeated with a minimum value for K_m to increase turbulent mixing in the event of weak wind shear and strong stability (Table 2). Simulations were also run with constant values of K_m . The magnitudes of the minimum values and the constant values are based on METCRAX II observations.

For the comparison with observations from VTMX, we use tethersonde data from IOP 1 on 2 October 2000, which featured the best-developed downslope flows according to Whiteman and Zhong (2008). During that IOP, soundings were made between approximately 1800 and 2130 mountain standard time (MST), with astronomical sunset at 1807 MST. Figure 3 shows the potential temperature deficit and along-slope wind profiles between 1830 and 2130 MST from three tethersondes operated along a line running down the slope together with simulated profiles after 6 h from the simulations listed in Table 2. With the TKE scheme, the simulation reproduces the observed surface inversion relatively well, but while the jet maximum wind speeds are of the correct magnitude, the drainage-flow depth is too

shallow. With the first-order scheme L, on the other hand, the simulated inversion is much stronger than the observed inversion. While the total drainage flow layer depth agrees relatively well with the observations, the jet maximum is too weak, and it occurs at lower heights than observed. The simulation with a modified first-order scheme B and the simulations with minimum values for K_m and with constant K_m agree better with the observations, closely reproducing the strength and depth of the surface inversion and the shape of the katabatic flow. All of the model simulations reproduce the slight increase of jet wind speeds with distance down the slope (not shown) as described by Whiteman and Zhong (2008). The close correspondence of the K0.15 simulation with the TKEK_m simulation indicates that K_m produced by the TKE scheme is generally below $0.15 \text{ m}^2 \text{ s}^{-1}$, so that the minimum value is used instead by the model.

While the focus of this paper is on two-dimensional simulations, we want to ensure that the selected model setup can also reproduce the katabatic flows observed upstream of the Meteor Crater. In contrast to the above comparison with VTMX data, which was for a completely unobstructed slope, the Meteor Crater slightly influences the upstream conditions. A brief comparison is therefore given of the katabatic flow from three-dimensional simulations with tethered-balloon soundings from two IOPs of

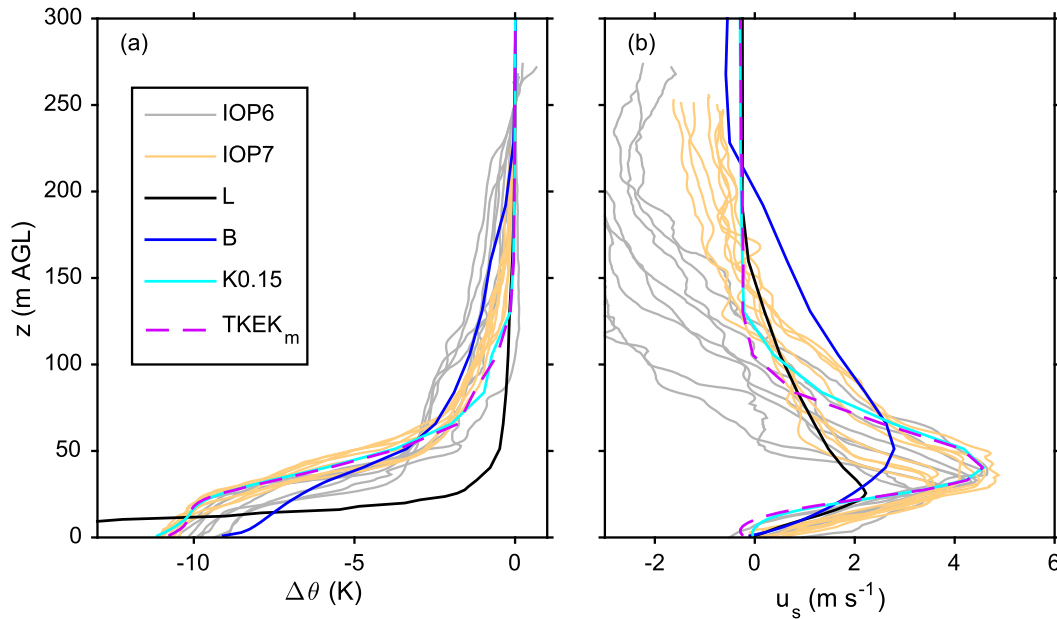


FIG. 4. As in Fig. 3, but for a comparison of 3D model simulations with tethered-balloon soundings from two nights (IOP6 and IOP7) of METCRAX II. Tethersonde profiles are from a 2-h window between 2300 and 0100 MST of the respective IOP.

METCRAX II (Fig. 4). The soundings were made at a site approximately 1 km upstream of the crater rim. Because of the upstream influence of the crater topography, this site is typically located within a cold-air pool that forms upstream of the crater and influences the katabatic flow. The effect of the cold pool is visible in the temperature profiles, which show a shallow 20–30-m-deep layer of relatively weak stability compared to the strong inversion above. A subset of four simulations was repeated with a three-dimensional, axisymmetric crater embedded within a two-dimensional mesoscale slope (Fig. 2a). The four simulations are indicated in Table 2. The crater basin is 150 m deep, has a 500-m-diameter basin floor, and is surrounded by a 40-m-high crater rim. Aside from the topography, the setup of these three-dimensional simulations is identical to the setup without initial wind speed described in section 2. In agreement with the above comparison with VTMX observations, the first-order scheme L performs worst. It produces a surface inversion that is too strong and too shallow and a drainage flow that is too weak. Because of the shallow inversion, the height of the jet maximum, which occurs near the top of the inversion layer, is also too low. While simulation B compared well with VTMX observations for the unobstructed, two-dimensional case, it overestimates the mixing in the three-dimensional case upstream of the crater, producing a weaker inversion and drainage flow than observed. The two simulations, K0.15 and TKEK_m, however, agree well with the observations, reproducing the depth and strength of both the

inversion and the downslope flow, including the shallow and weakly stable cold pool near the surface. The simulated downslope flows reverse sign to a weak upslope component (anti-wind) between 100 and 150 m AGL. The magnitude of this anti-wind is similar to the observations during IOP 7 and also to the observations from VTMX (Fig. 3). In contrast to the simulations, however, the measured downslope flows are impacted by external influences, as is obvious from the more than 2 m s^{-1} anti-winds during IOP6 (Fig. 4).

During METCRAX II, a 50-m-high tower approximately 1.6 km upstream of the crater was instrumented with sonic anemometers at 5-m intervals (Lehner et al. 2016). Vertical profiles of eddy diffusivities K_m and heat conductivities K_h were calculated from the data (Fig. 5). The values are not constant with height, but decrease slightly within the lowest approximately 20 m AGL, particularly K_h . Near the surface, K_m ranges mostly between 0 and $0.2 \text{ m}^2 \text{ s}^{-1}$. Heat conductivity has a somewhat larger spread toward the higher end near the surface. The magnitude of the observations, however, supports the good agreement between the observed temperature and wind profiles with simulations using $K_m = K_{\min} = 0.15 \text{ m}^2 \text{ s}^{-1}$. Haiden (2003) used observed temperature and katabatic flow profiles from VTMX IOP4 to determine K based on the Prandtl solution and found even smaller values, with $K_m = K_h = 0.026 \text{ m}^2 \text{ s}^{-1}$. Based on our model comparisons, we are using the TKE scheme with a minimum value of $0.15 \text{ m}^2 \text{ s}^{-1}$ for all of the simulations described in the remainder of this paper.

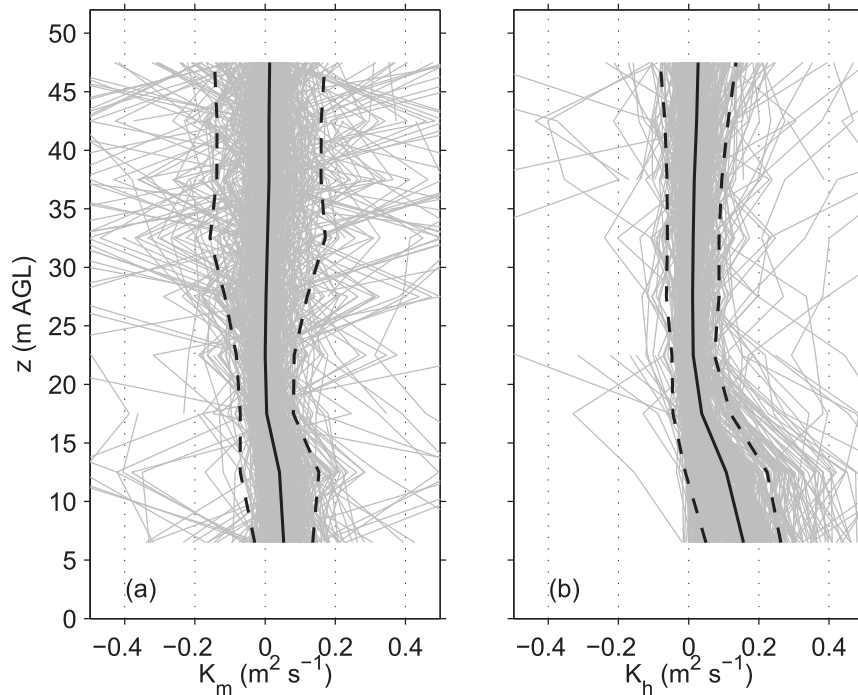


FIG. 5. Vertical profiles of (a) K_m and (b) K_h from observations during METCRAX II. Profiles were calculated for IOPs 1–4 and 6–7 between 2200 and 0400 MST (gray lines). The black solid lines are mean profiles, and the black dashed lines are the mean plus or minus one standard deviation. The value of K_m was calculated based on the east–west wind component u and the turbulent flux $\overline{u'w'}$.

While this scheme is basically identical to a constant K_m scheme for the simulation of the katabatic flows, it has the advantage that it can produce additional and more realistic mixing in the wave regions over the basin, where the flow becomes more turbulent.

Surface cooling and subsequently katabatic flow forcing are also a function of the surface-layer parameterization: that is, the turbulent fluxes between the ground and the atmosphere. These fluxes are, in turn, dependent on the atmospheric conditions and are thus also influenced by the turbulence parameterization. While the simulated surface heat flux is too low compared to observations (not shown), the model reproduces the near-surface air temperatures correctly (Figs. 3, 4). We are accepting the deficiency in correctly reproducing the surface heat flux as we put our emphasis on reproducing correct near-surface air temperatures and correct temperature and wind profiles.

4. Flow over a basin

a. Basin depth

Having verified that the model produces realistic upstream flow conditions, we insert a 500-m-wide basin in the center of the mesoscale slope. Simulations are made

for basin depths that range from 5 to 150 m, with 150 m being close to the depth of the Meteor Crater (experiment EXPDEP; Table 1). Cross sections of streamwise wind speed u and potential temperature are shown in Fig. 6.

For a shallow, 5-m-deep basin, the flow follows the underlying terrain, sweeping the basin atmosphere (Fig. 6a). The jet maximum wind speeds are almost constant across the basin. The flow regime changes for a 10-m-deep basin (Fig. 6b). A stationary wave forms at the downstream end of the basin. A weak acceleration of the flow into the basin occurs, with a wind speed minimum at the location of the wave. Increasing the basin depth further to 15 (not shown) and 20 m (Fig. 6c), a wave forms with two wave crests. Negative u velocities underneath the wave crests suggest the formation of rotors, which is confirmed by closed streamlines in the positive vorticity region under the first wave crest (Fig. 7). The layer of high positive vorticity below the katabatic jet maximum upstream of the basin thins as the flow descends into the basin. It then separates from the surface at the leading edge of the upstream wave, similar to the simulations by Doyle and Durran (2002, 2007) for flow over a ridge.

A wave with two wave crests forms also for larger basin depths of 50 and 100 m (Figs. 6d,e), but the wind

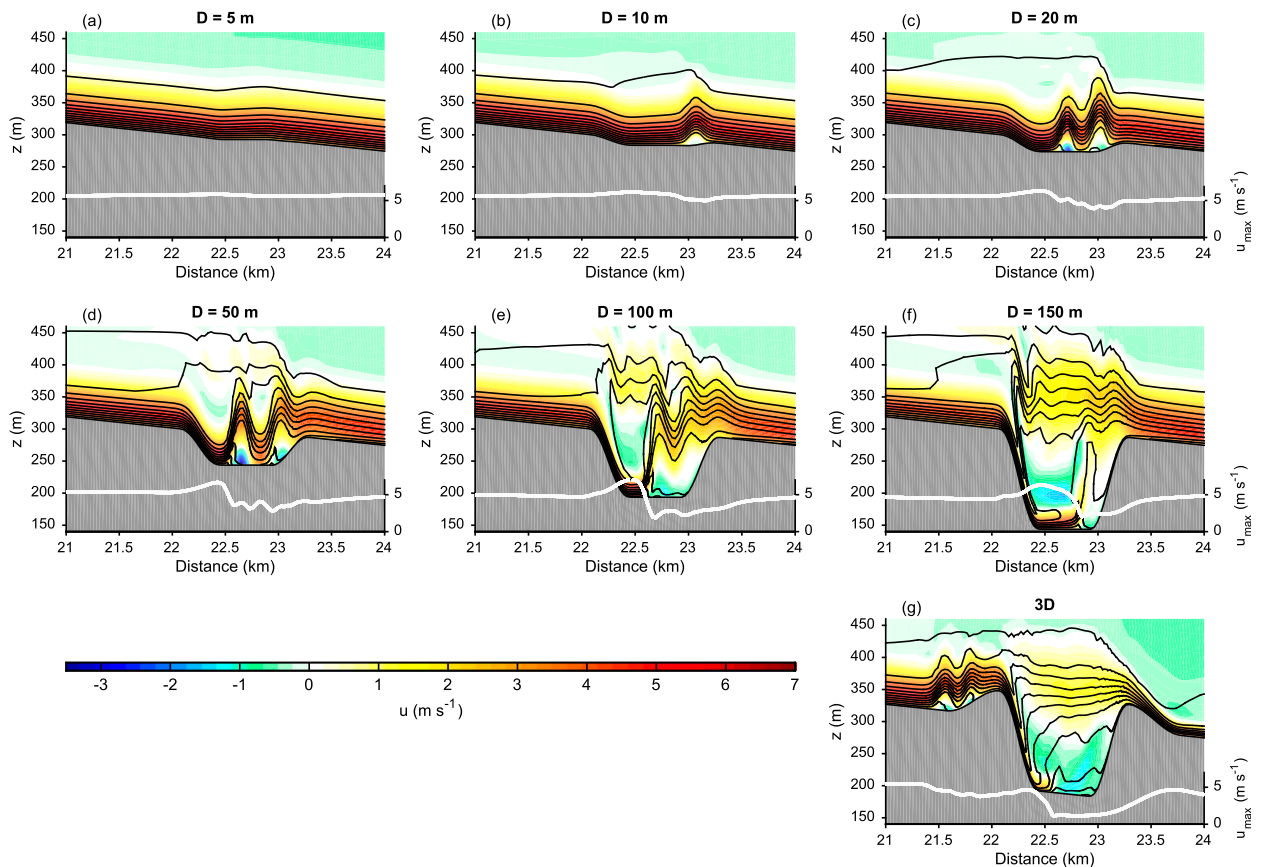


FIG. 6. (a)–(f) Vertical cross sections after 6 h of the streamwise wind component (colors) and potential temperature (black contour lines) for simulations with 0 m s^{-1} initial wind and different basin depths of 5, 10, 20, 50, 100, and 150 m. (g) A west–east cross section through the three-dimensional simulation TKEKm. Isentropes are at 1-K intervals. The white line shows the jet maximum wind speed along the slope.

speeds in the wave region decrease with increasing basin depth, as does the strength of the recirculation underneath the second, downstream wave crest for basins deeper than 20 m. The wave motion is confined to the inversion and katabatic jet, which separates from the surface over the basin floor to form the wave and reconnects with the katabatic jet over the downstream mesoscale slope. The flow clearly thins and accelerates along the upstream basin sidewall, as expected for a downslope-windstorm-type flow. For the 50-m-deep basin, the solution shows an almost vertical isentrope near the edge of the upstream sidewall, indicative of wave breaking (Fig. 6d). The wave breaking region above the upstream sidewall becomes more prominent, with increasing basin depths of 100 and 150 m, for which the regime changes again (Figs. 6e,f). A hydraulic-jump-type solution forms over the basin floor. A similar solution with a wave-breaking region over the lee slope and a hydraulic jump downstream is also present in the two-dimensional simulations over a single hill by Lin and Wang (1996) and Vosper (2004). The model simulations, however, do not capture the wave breaking well,

but produce overturning isentropes over the upstream sidewall, suggesting that the eddy diffusivities and thus TKE produced by the turbulence parameterization are too low.

While a wave is still present downstream of the jump in the 100-m-deep basin, it is completely absent in the 150-m basin. The originally surface-based inversion is split into two parts over the basin, with one part remaining attached to the topography in connection with the flow descending into the basin. The second region of strong stratification is located near the top of the basin, with somewhat weaker stability than near the surface. The region between the surface-based inversion and the top of the basin is well mixed. While the jet in the wave regime is continuous between the sloping plains upstream and downstream of the basin (Fig. 6d), the hydraulic jump forms a discontinuity, in which the jet splits and the flow penetrating into the basin does not connect directly with the katabatic flow over the downstream mesoscale slope (Fig. 6f).

A cross section through the basin from the three-dimensional simulation TKEKm is included in Fig. 6g

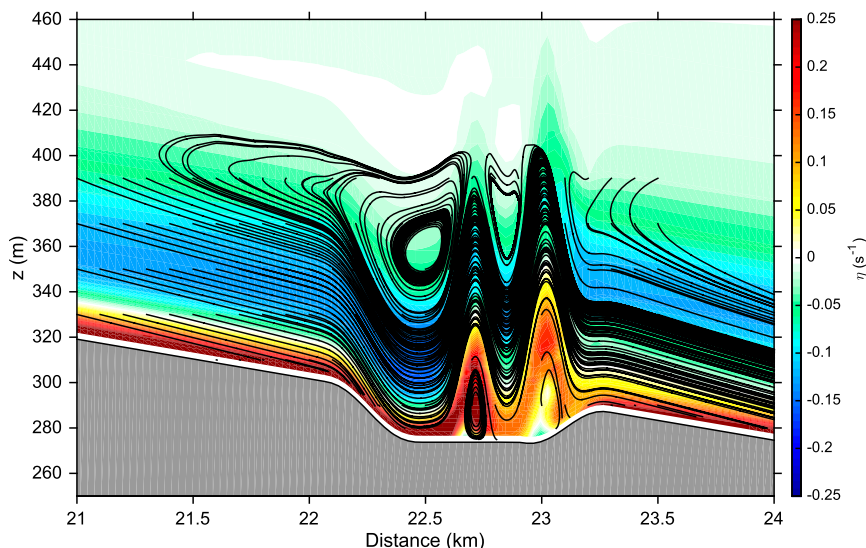


FIG. 7. Vertical cross section of cross-slope vorticity (color shaded) and streamlines for a 20-m-deep basin with initial wind speeds of 0 m s^{-1} .

for comparison with the two-dimensional simulation with a 150-m-deep basin (Fig. 6f). A 40-m-high rim surrounds the basin in the three-dimensional simulation, which leads to the formation of waves upstream of the basin in contrast to the two-dimensional simulations. Within and above the basin, however, the same flow splitting occurs, as can be seen in Figs. 6e and 6f, which has been defined here as a hydraulic jump regime. The two-dimensional simulations are thus in good qualitative agreement with the three-dimensional simulation.

The solutions for the 50–150-m-deep basins agree also qualitatively with the wind field derived from dual-Doppler lidar observations in a vertical cross section through the Meteor Crater during METCRAX II (Fig. 1). During periods of downslope-windstorm-type flows a wavelike flow was sometimes observed with a wave crest over the center of the crater, similar to Fig. 6d. During other periods, the flow split, with part of the flow descending along the terrain and part of the flow going over the crater basin, similar to Fig. 6e.

b. Background wind speed

The initial solution for the 100-m basin shows a hydraulic jump (not shown) similar to the 150-m basin. The flow, however, evolves into a wave-type solution by deepening the wave downstream of the hydraulic jump as the katabatic winds increase (Fig. 6e), suggesting that wind speed also affects the flow regime. To include this parameter in the analysis, simulations with basin depths of 10–150 m were repeated with initial, homogeneous wind speeds of 2, 5, 7, 10, and 15 m s^{-1} in the direction of the katabatic flow (experiment EXPSPD; Table 1). The

katabatic flow is thus enhanced by the background wind, which increases the jet maximum wind speed u_{max} compared to the cases initialized with a 0 m s^{-1} wind speed (Fig. 8b). In addition to increased u_{max} , the wind shear above the jet maximum is reduced by the presence of background winds. The background wind above the katabatic flow decreases slightly with time. For example, the initial 15 m s^{-1} wind has decreased to approximately 13 m s^{-1} at the end of the 6-h simulation (Fig. 8b). The deceleration is a model artifact related to a strong damping of the flow near the bottom of the damping layer. Since the reduction in wind speed above the katabatic flow is larger for strong initial winds of 10 and 15 m s^{-1} than for weaker initial winds, the wind speed profiles for the 7 and 10 m s^{-1} cases are relatively similar at the end of the 6-h simulations. The stronger winds, however, have little effect on the stability of the near-surface layer, which remains large, with $N > 0.1 \text{ s}^{-1}$ at the surface (Fig. 8a).

The simulations are summarized in Fig. 9. Results for the 15-m-deep basin are very similar to the results for the 20-m-deep basin and are therefore omitted from the figure. For the 10–20-m-deep basins the regime changes from a wave ($0\text{--}2 \text{ m s}^{-1}$ background wind speed) with one wave crest (10 m) and two wave crests (15–20 m) to a sweeping of the basin (5 m s^{-1} and more). For the 50-m-deep basin, the regime changes from a wave with two wave crests ($0\text{--}2 \text{ m s}^{-1}$) to a wave with one wave crest at the downwind end of the basin (5 m s^{-1}) and eventually to a sweeping flow (7 m s^{-1} and more). For the 100- and 150-m-deep basins, the hydraulic jump over the upstream sidewall disappears with increasing wind speeds

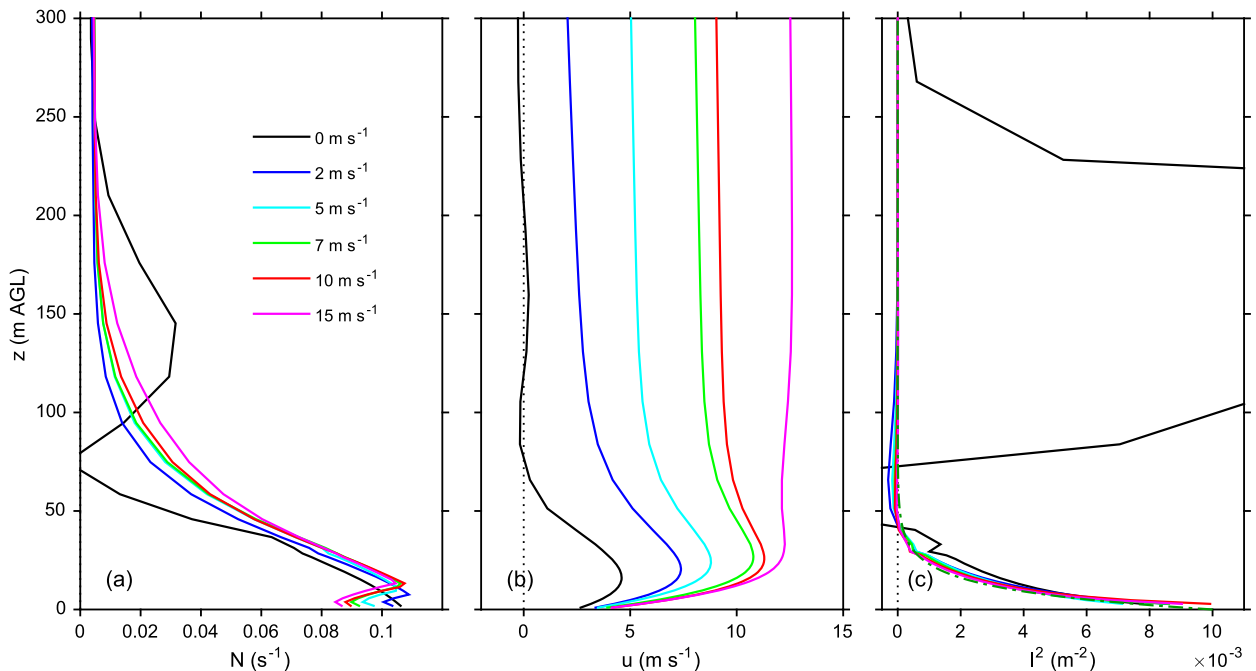


FIG. 8. Vertical profiles of (a) N , (b) streamwise wind velocity u , and (c) the Scorer parameter l^2 after 6 h of simulation time for a 150-m-deep basin and varying initial wind speeds of 0, 2, 5, 7, 10, and 15 m s^{-1} . Profiles are taken approximately 900 m upstream of the basin. The green dashed–dotted line in (c) shows an exponential approximation of the profiles used in section 5.

(not visible in all of the 286-K isentrope in Fig. 9). Instead, the location of the hydraulic jump over the basin floor moves farther upstream. For wind speeds of 7 m s^{-1} or more, a wave with one crest forms over and downstream of the downstream basin sidewall. While the wave is located over the basin for a 50-m-deep basin and initial wind speeds of 5 m s^{-1} , it is found farther downstream above the downstream basin sidewall and downstream mesoscale slope for the deeper basins. Simulations with hydraulic jumps show a much stronger flow variability with time downstream of the hydraulic jump compared to upstream and compared to other simulations. With strong winds of 15 m s^{-1} and a deep basin of 100 m or more, the flow separates at the upstream crater edge, producing a wake near the upstream basin sidewall. The results for the deep basins agree with the findings of Vosper (2004) and Sheridan and Vosper (2006), who found that the wave amplitude decreases with increasing Froude number (increasing wind speed) for a two-layer atmosphere and a two-dimensional flow over a hill so that the flow regime changes from a hydraulic jump to gravity waves and eventually to a no-wave regime.

Some simulations show a transition from one regime to another or do not reach a steady solution and keep transitioning back and forth between two regimes. An example is the simulation with a 10-m-deep basin and

2 m s^{-1} initial wind speeds. Figure 9 shows that for small u_{max} (purple colors), which occur earlier in the simulation, a wave with two crests is present over the downstream basin end. As katabatic wind speeds increase with time, the solution transitions to a wave with a single wave crest at the end of the 6-h simulation time (cyan colors). Another example is shown in Fig. 10 for a 100-m-deep basin with 2 m s^{-1} initial wind, which transitions between a hydraulic jump and a wave with two wave crests. At 310 min, a wave with two wave crests is present over the basin with recirculation underneath the wave crests (Fig. 10a). During the next 10 min (note that all figures are based on 10-min averages), the wave is replaced by a hydraulic jump at the foot of the upstream sidewall (Fig. 10b). Ten minutes later, the flow has again organized into a wave. (Fig. 10c).

The different flow regimes also affect the basin cold pool, which forms because of nocturnal cooling, to different degrees. To quantify the effects on cold-pool strength and on flow accelerations and decelerations over the basin, the vertically integrated heat deficit and momentum are calculated (Fig. 11). The heat deficit

$$c_p \int_0^{500} \rho(z) [\theta(500) - \theta(z)] dz \quad (2)$$

and momentum

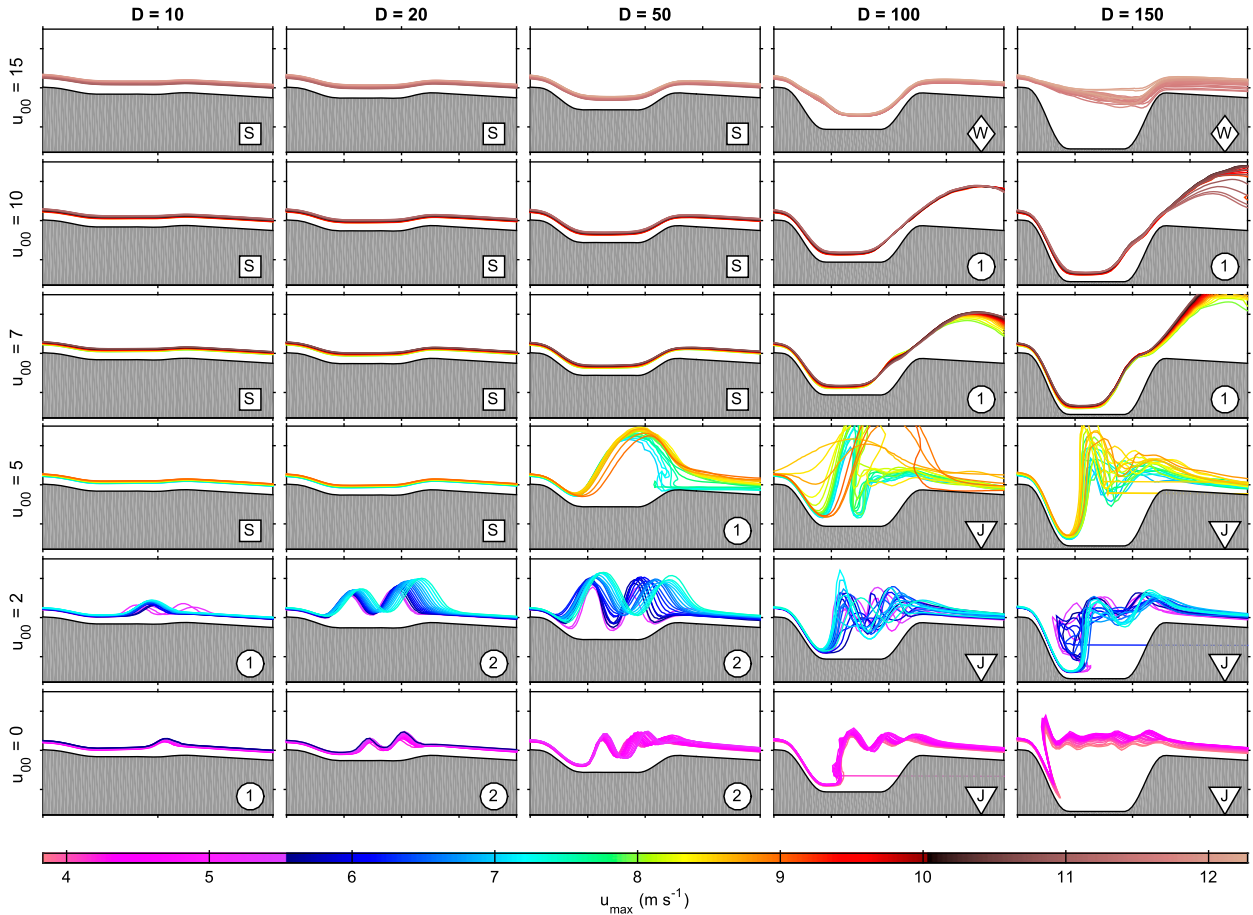


FIG. 9. The 286-K isentropes at 10-min intervals between 3 and 6 h for simulations with 500-m-wide basins, varying depth (columns from $D = 10$ to 150 m), and varying initial wind speed (rows, $u_{00} = 0$ –15 m s^{-1}). Line color indicates the jet maximum wind speed approximately 900 m upstream of the basin. The symbols in the bottom-right corner of each panel indicate the resulting flow regime: sweeping (S), wake (W), wave with one wave crest (1), wave with two wave crests (2), and hydraulic jump (J).

$$\int_0^{500} \rho(z) |\mathbf{v}(z)| dz \quad (3)$$

are integrated between the surface and 500 m AGL. Here, $c_p = 1004 \text{ J kg}^{-1} \text{ K}^{-1}$ is the specific heat capacity of air at constant pressure, $\rho(z)$ is the air density at height z above ground level, $\theta(500)$ is the potential temperature at 500 m AGL, and $|\mathbf{v}|$ is the wind speed calculated from the streamwise and vertical components. At 500 m AGL, the influence of the underlying terrain has mostly subsided. The vertically integrated heat deficit and momentum were calculated for the grid points indicated in Fig. 2b and averaged over the upstream, basin, and downstream areas. The basin and downstream values were normalized by the upstream values at each output time. Because there was little change with time after 3 h, the normalized values were averaged between 3 and 6 h. In the sweeping regime (e.g., strong winds and shallow basins), no cold-air pool

builds up in the basin. The heat deficits in the basin and downstream are almost identical to the heat deficit over the upstream mesoscale slope. In the hydraulic jump and wave regimes, the heat deficit in the basin is up to more than 4 times larger than upstream. The cold air that forms over the basin surface can accumulate underneath the wave or downstream of the hydraulic jump. The largest heat deficit occurs generally with $u_{00} = 2 \text{ m s}^{-1}$, with the exception of the 100-m-deep basin, for which the heat deficit peaks at $u_{00} = 5 \text{ m s}^{-1}$. This particular simulation is at the transition between a hydraulic-jump regime and a wave regime with one crest, with an extremely deep cold-air dome over the basin, which, however, is not captured by the 286-K isentropes in Fig. 9. The simulation with a wave with one crest over the downstream basin sidewall (10-m-deep basin with 0 m s^{-1} initial wind speeds) does not show an increased heat deficit in the basin. This, however, is due to the selection of basin grid points (see Fig. 2), which excludes

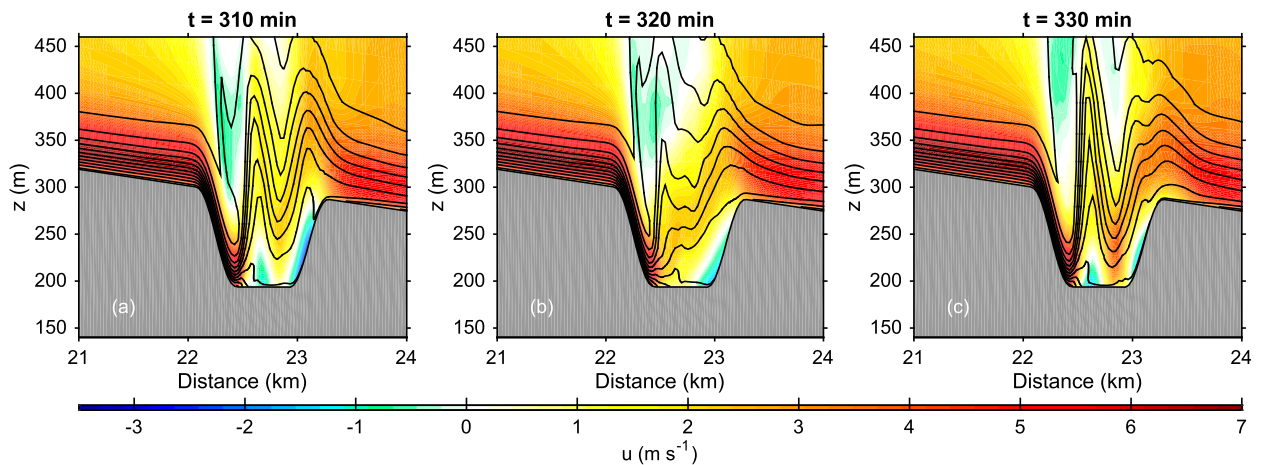


FIG. 10. Vertical cross sections of the streamwise wind velocity (colors) and potential temperature (black contour lines) for a 100-m-deep basin and an initial wind speed of 2 m s^{-1} after (a) 310, (b) 320, and (c) 330 min of simulation time. Isentropes are at 1-K intervals.

the sidewall region underneath the wave crest, where a small cold-air dome exists. The simulations with 100–150-m-deep basins also show an increased heat deficit downstream of the basin because of the downstream extent of the wave. The vertically integrated momentum shows that without a background wind the flow accelerates into the basin, particularly for basins deeper than 20 m. For the three shallow basins, the acceleration is

weak. With increasing wind speeds of 2 m s^{-1} the acceleration turns into a weak deceleration for shallow basins. With even stronger winds the flow inside the basin is almost identical to the flow upstream, with a weak acceleration downstream of the basin. In the hydraulic-jump regime for the deep basins, the flow decelerates strongly in the basin. This is also obvious from Figs. 6e and 6f, which show the comparatively

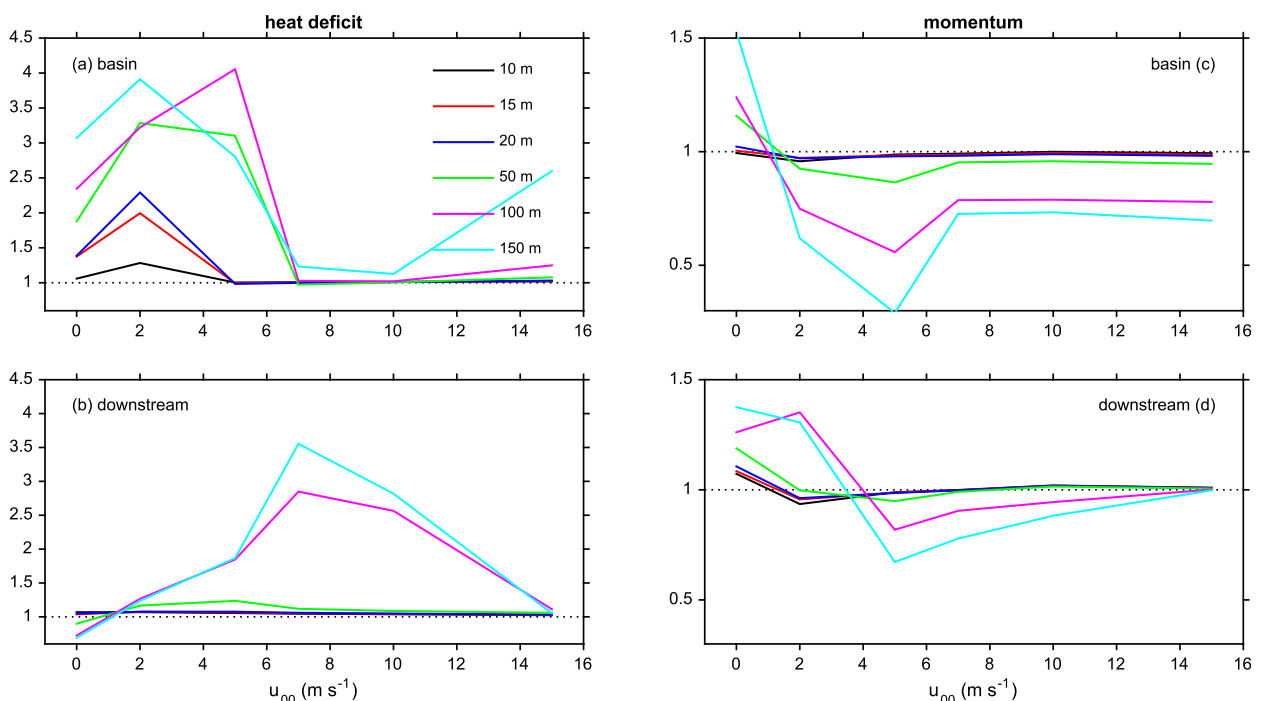


FIG. 11. Vertically integrated (a),(b) heat deficit and (c),(d) momentum as a function of initial wind speed u_{00} (colored lines) and basin depth D for (a),(c) the basin floor and (b),(d) the slope downstream of the basin (see Fig. 2 for grid point locations). Values are normalized by upstream values. See text for details.

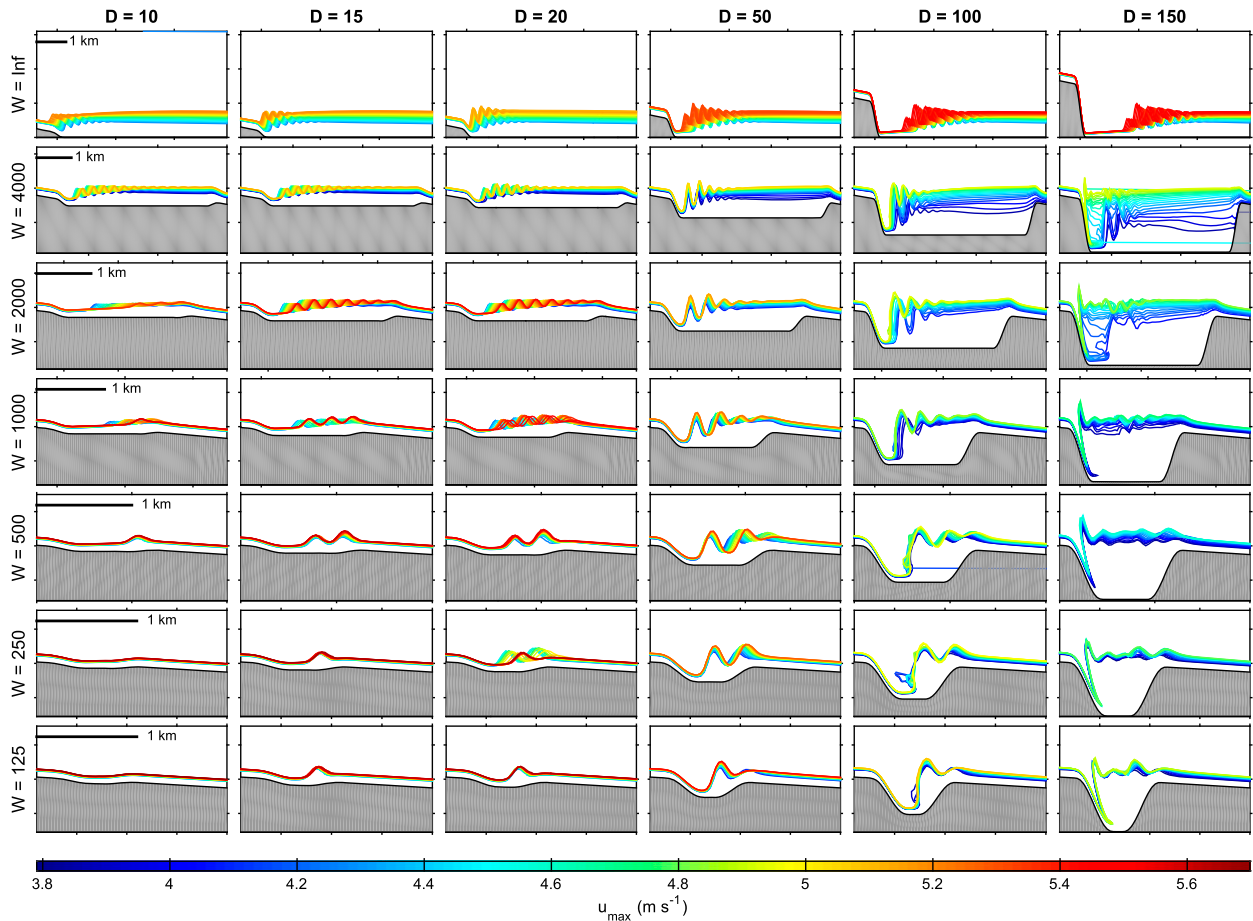


FIG. 12. The 286-K isentropes at 10-min intervals between 3 and 6 h for simulations with varying basin depths (columns, from $D = 10$ to 150 m) and widths (rows, W from 125 to ∞ m) and 0 m s^{-1} initial wind speed. Line color indicates the jet maximum wind speed approximately 900 m upstream of the basin. Note the change in the horizontal scale with increasing basin width (indicated by the horizontal black line in the top-left corner of each panel in the first column).

weak winds in the rather turbulent hydraulic-jump region.

c. Basin width

The resulting regimes for 0 m s^{-1} initial wind speeds do not change if the basin width is varied, but the basin width affects the number of wave crests that form in the wave regime. Figure 12 summarizes simulations with basin widths of 125 m to semi-infinitely wide basins and depths of 10–150 m (experiment EXPWID; Table 1). The simulations with a basin depth of 10–50 m produce a wave over the basin, whereas the simulations with a deeper basin of 100–150 m produce a hydraulic-jump-type solution, indicating that the wave amplitude and thus the resulting flow regime are determined by the basin depth and do not depend on the basin width. In the wave regime ($D = 10\text{--}50$ m), the number of wave crests over the basin depends both on the basin width and depth. For narrower basins, the wave is confined to the

basin so that the number of wave crests is limited by the basin width. Generally, the number of wave crests increases with increasing width so that a long wave train is produced over wide basins. However, the wave amplitude also decays with distance downstream because of viscous effects so that, for large basins (e.g., the 4000-m-wide basin), the number of wave crests is not limited by the downstream topography but by the decay of the waves, resulting in a similar solution to the infinitely wide basin. The decay of trapped lee waves downstream of a mountain as a result of the absorption of downward energy by the boundary layer was shown by Jiang et al. (2006) using theory and numerical simulations. The number of wave crests also increases with increasing basin depth, for example, from 0 to 1 and 2 wave crests for a 250-m-wide basin and basin depths of 10–50 m. At the same time, the decay of wave amplitude with distance is also stronger for the 50-m-deep basin than for the shallower basins: for example, for the 1- and 2-km-wide basins.

5. Discussion

The presence of standing waves for certain parameter combinations (Fig. 9) suggests the presence of lee waves (Scorer 1949). For two-layer flow characterized by constant values of the Scorer parameter

$$l^2 = \frac{N^2}{u^2} - \frac{1}{u} \frac{d^2 u}{dz^2} \quad (4)$$

in each layer, the condition for standing lee waves is

$$l_1^2 - l_2^2 > \frac{\pi^2}{4z_1^2}, \quad (5)$$

where l_1 and l_2 are the values of l in the lower and upper layers, respectively, and z_1 is the thickness of the lower layer. In the present case, the Scorer parameter (Fig. 8c) suggests the possibility of wave trapping, since $l_2 \approx 0$.

To establish the possibility of lee waves for a more complex flow such as that shown in Figs. 8a and 8b, one must use a more sophisticated test. The presence of lee waves is only possible if internal gravity waves can propagate upstream: that is, if the flow is subcritical. To determine the criticality of the flow shown in Fig. 8, we make use of the test devised by Benjamin (1962, pp. 600–601). Approximating the profiles of l^2 in Fig. 8 with $l^2(z) = l_s^2 e^{-z/\delta}$, the condition for lee waves becomes

$$l_s \delta > 1.2. \quad (6)$$

Using $\delta = 10$ m and any of the values for l_s in Fig. 8 shows that (6) is not satisfied and therefore lee waves are not expected. The derivation of (6) is shown in the appendix.

The Scorer criterion is equivalent to the criterion for an internal gravity wave to propagate upwind: that is for $u = c_-$, where c_- is the fastest possible upstream-propagating wave speed. To make further progress, the evolution of flow criticality in the streamwise direction is examined using existing theories for a simpler, two-layer atmosphere. The profiles of N and u (Figs. 8a,b) suggest the simplification of a constant N in the lower layer with $N = 0$ in the upper layer and $u = U$ constant throughout the entire depth; in this case, $c_- = 2Nz_1/\pi$ (Baines 1995, p. 281) and the criterion (5) can be restated as $U/c_- < 1$, which is the definition of subcritical flow. As the Scorer criterion is not satisfied, the implication is that the katabatic flows upwind of the valley in the present simulations are supercritical, and a transition to subcritical conditions is necessary farther downstream to explain the occurrence of the simulated waves.

This simplified two-layered flow also satisfies the conditions for the application of Long's equation to flow over topography by Smith (1985, hereafter S85). Although the

focus of S85 is on flow over hills, the solutions for flow over a hill into a valley (S85's Fig. 4) are also considered. In the present case, we are concerned with flow from a plain directly into the valley with no intervening hill; this puts our cases in the left half of S85's Fig. 2. This half of his figure is reproduced in Fig. 13. One can see in Fig. 13 that only the curves $n = 0-3$ give a continuous thinning of the layer depth (and accelerating flow) with increasing valley depth, while for $n > 3$ the stratified layer thickens with increasing valley depth. The reason for this behavior is that the $n = 3$ curve corresponds to $\hat{H}_0 = Nz_1/U = \pi/2$, which is precisely $U/c_- = 1$ (critical flow). Curves $n < 3$ and $n > 3$ thus correspond to supercritical and subcritical flow, respectively. It can be shown from the S85 solution that the supercritical flow entering the valley from a plain will remain supercritical with no further transitions in the absence of incompatible downstream conditions. This situation is exactly analogous to that encountered in shallow-water theory (Baines 1995, p. 39).

Although the behavior of a supercritical flow entering a valley is clear from the foregoing considerations, the downstream end of the valley presents a change in local conditions to which the supercritical flow must adjust. Armed with the ideas outlined above, we devised a simple analysis of the solutions shown in Fig. 9 by computing the local wave speed

$$c_x(x, t) = u(x, t) - \frac{2N(x, t)z_1(x, t)}{\pi}, \quad (7)$$

corresponding to the hypothetically fastest upstream-propagating wave. In (7), we estimate the parameters as follows: $u(x, t)$ and $N(x, t)$ are approximated by the maximum wind speed $u_{\max}(x, t)$ and stability $N_{\max}(x, t)$ in the vertical column, respectively, and z_1 is approximated by the depth of the layer for which $N(x, t)$ is larger than 25% of $N_{\max}(x, t)$. The threshold of 25% was selected based on a subjective identification of the inversion top in the upstream profiles shown in Fig. 8a. The results are shown in the Hovmoeller diagrams in Fig. 14, which are organized to correspond to the matrix of solutions shown in Fig. 9. The top row of Fig. 14 clearly shows that for large wind speeds the flow is everywhere supercritical, and no waves appear in the solutions (top row of Fig. 9). For lower wind speeds (the middle rows of Figs. 9 and 14), c_x begins to exhibit values near zero, suggesting the possibility of standing waves; in particular, the $u_{00} = 7 \text{ m s}^{-1}$ row shows a transition with increasing basin depth from clearly positive values to areas with near-zero values. The two bottom rows suggest conditions that are marginally critical and, accordingly, even the shallower basins have waves forming in the generally subcritical conditions produced on the downstream basin sidewall.

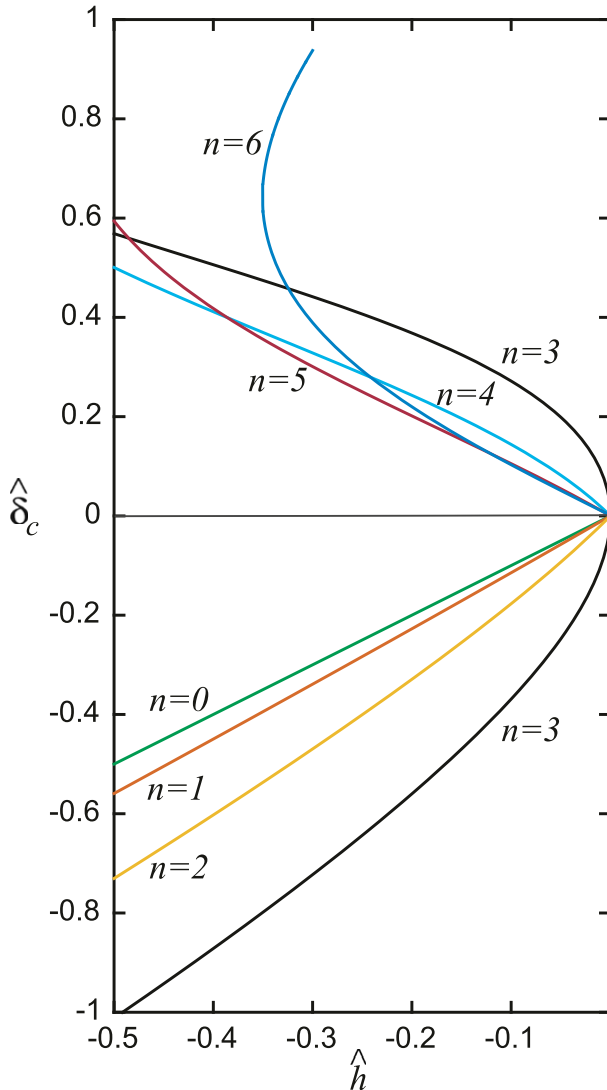


FIG. 13. Vertical deflection of the critical streamline $\hat{\delta}_c = N\delta_c/U$ as a function of terrain height $\hat{h} = Nh/U$. Negative values of \hat{h} indicate a descent into a valley from a plain ($h = 0$). Negative and positive values of $\hat{\delta}_c$ correspond to a thinning and thickening of the stable layer, respectively. The individual curves are for different depths of the upstream stable layer ($\hat{H}_0 = Nz_1/U = n\pi/6$). Adapted from Smith (1985), with additional curves calculated in Durran and Klemp (1987).

Calculating the horizontal wave speed similar to Fig. 14 for experiment EXPWID (not shown) shows again marginally critical or supercritical conditions upstream, which transition to subcritical conditions over the basin, even over the infinitely wide basins as the flow adjusts to the stagnant or weak flow over the flat basin floor. In contrast to the simulations with 500-m-wide basins (section 4b), increased initial wind speeds do not result in a sweeping flow in the case of infinitely wide basins (not shown). Instead, waves form downstream, away from the upstream

sidewall, with the distance of the waves from the upstream crater sidewall increasing with increasing wind speeds. Only with a 15 m s^{-1} initial wind, for which the flow is clearly supercritical everywhere (not shown), does a sweeping flow develop downstream.

6. Conclusions

The object of this work is to study flow over a basin and the impact of basin size and upstream flow and stability conditions on the resulting flow regimes using two-dimensional model simulations of flow over an idealized basin. The work is motivated by a desire to understand the formation of nocturnal downslope-windstorm-type flows in Arizona’s Meteor Crater. Downslope-windstorm-type flows at the Meteor Crater occur regularly as a result of mesoscale katabatic winds that form over the upstream low-angle slope and flow over the crater. The model simulations were thus designed to reproduce a realistic surface-based inversion and katabatic flow due to radiative cooling above a slope upstream of the basin and to evaluate the flow response over basins of varying size. In addition, we modified the katabatic flow strength by initializing the simulations with varying uniform background wind speeds.

Initial model simulations and observations from METCRAX II showed that the flow response over the basin strongly depends on the upstream flow profile, specifically the depth and strength of the katabatic jet. The simulated katabatic flow was compared to observations from the METCRAX II and VTMX field campaigns over two low-angle slopes. Simulations with different turbulence parameterizations were tested, including a TKE and several first-order and constant- K schemes. The comparison showed that the turbulence parameterization strongly affects the strength and shape of the drainage flow and the surface-based inversion. The particularly strong stability near the surface reduces turbulent mixing in all schemes that include a stability dependence. Based on the comparison with observational data, a TKE scheme with a minimum eddy diffusivity and heat conductivity of $0.15 \text{ m}^2 \text{ s}^{-1}$ was chosen.

A series of simulations with increasing basin depth (10–150 m) and increasing initial wind speed ($0\text{--}15 \text{ m s}^{-1}$) was run. The initial wind speed modifies the katabatic jet profile by increasing the jet maximum and reducing the wind shear above the jet maximum. The resulting flow responses were classified into four different regimes: (i) wakes over the upstream basin sidewall, (ii) a sweeping of the basin atmosphere, (iii) waves over the basin, and (iv) stagnation over the upstream basin sidewall and a hydraulic jump. A wake occurs only for strong initial winds of $u_{00} = 15 \text{ m s}^{-1}$ and the deep

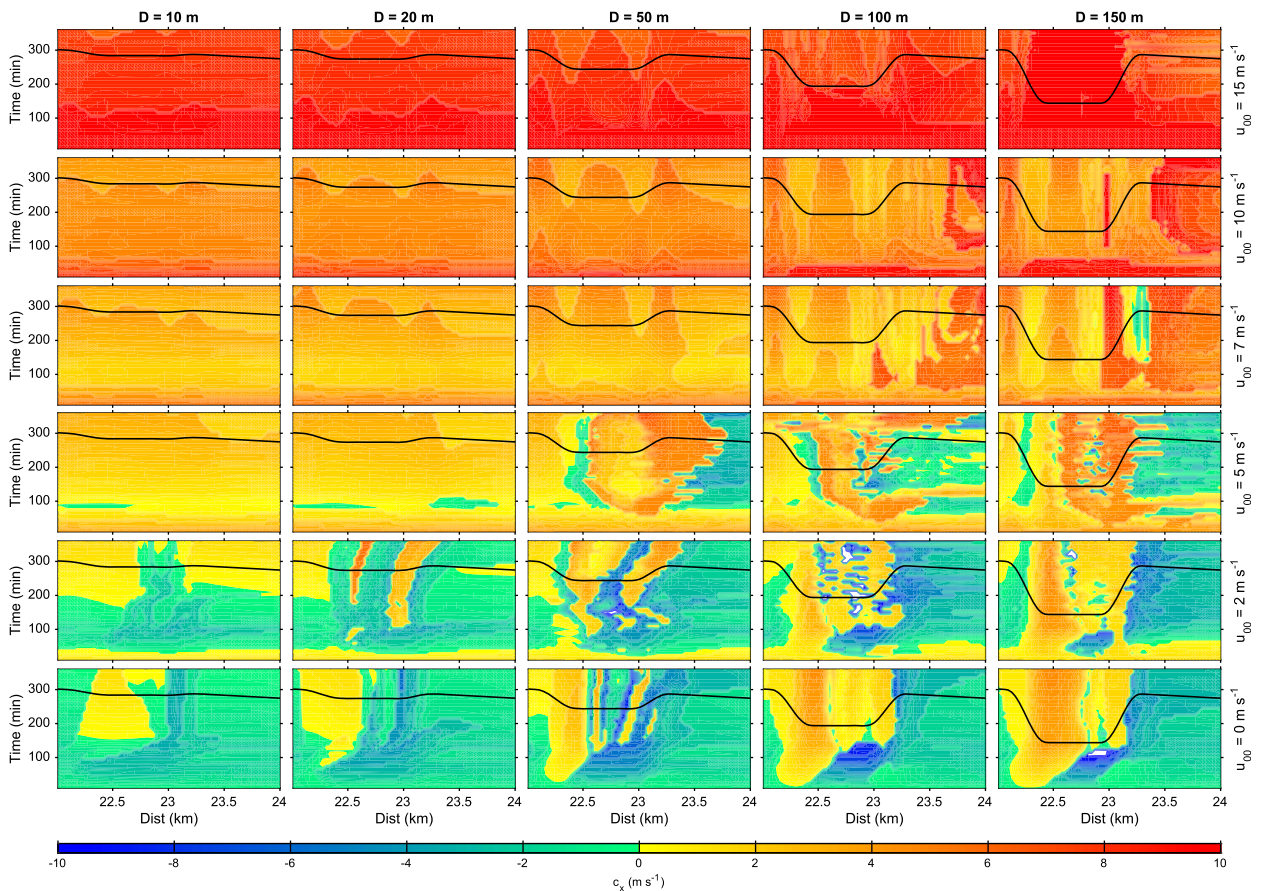


FIG. 14. Hovmöller diagrams of the horizontal phase speed for simulations with 500-m-wide basins, varying depth (columns, from $D = 10$ to 150 m), and varying initial wind speed (rows, from $u_{00} = 0$ to 15 m s^{-1}). The black line shows the model topography.

100- and 150-m basins. A sweeping of the basin is found in simulations with $D \leq 20 \text{ m}$ and $u_{00} \geq 5 \text{ m s}^{-1}$ and with $D = 50 \text{ m}$ and $u_{00} \geq 7 \text{ m s}^{-1}$, in which the flow is supercritical everywhere. For lower wind speeds, the flow becomes locally subcritical, and waves form over the basin, with the waves being confined to the basin region. The number of wave crests depends on the width of the basin. Another series of simulations with varying basin widths showed that the downstream extent of the wave is limited by either the length of the basin or by the decay of the wave as a result of energy loss in the case of large basins. For sufficiently deep basins ($D \geq 100 \text{ m}$) and low wind speeds ($u_{00} \leq 5 \text{ m s}^{-1}$), the flow stagnates over the upstream basin sidewall, producing wave breaking and a hydraulic jump over the basin floor. This regime is similar to the observations from the Meteor Crater, consistent with the depth of the crater basin (approximately 170 m) and with the typical upstream maximum wind speeds of about 5 m s^{-1} .

The relatively frequent occurrence of the observed downslope-windstorm-type flows at the Meteor Crater

seems thus to be the result of a fortuitous combination of the right crater size and upstream flow conditions produced by the katabatic flow. The depth and strength of katabatic flows have been found to strongly depend on the slope angle, with typically deeper and stronger katabatic flows over low-angle slopes, such as the one upstream of the Meteor Crater (Zardi and Whiteman 2012). A steeper upstream slope would thus likely produce a shallower and weaker katabatic flow, which would impact the resulting flow regime and may reduce the frequency of downslope-windstorm-type flows at the Meteor Crater. Observations from the Meteor Crater (Lehner et al. 2016) and initial model simulations with a shallow katabatic flow (not shown) indicate a much weaker flow response over the crater compared to a deeper katabatic flow.

The simulations summarized in Fig. 9 show that a variety of different flow regimes is possible when air flows over a basin or valley. The parameter space covered in this study is limited to the flow conditions observed upstream of the Meteor Crater (e.g., Lehner et al.

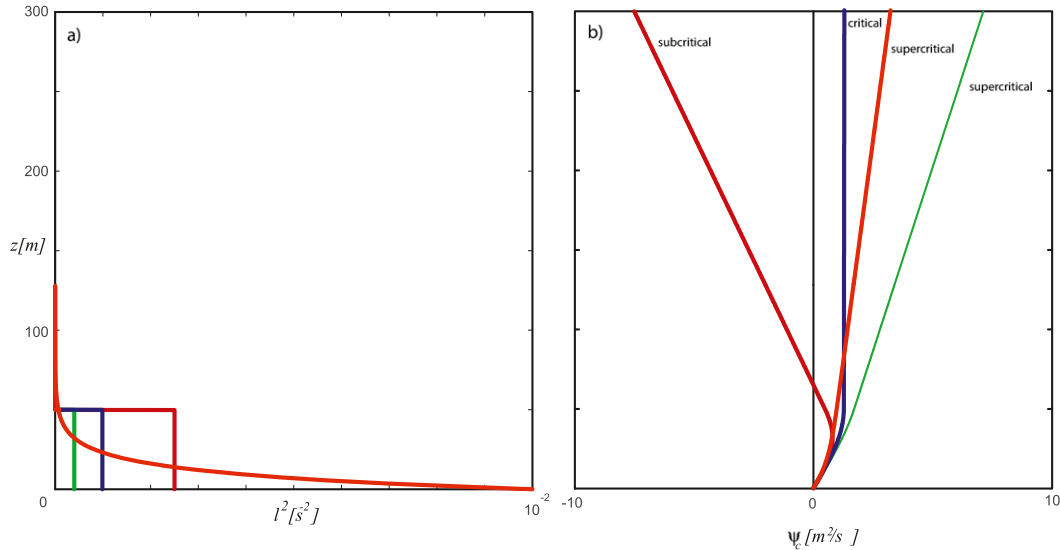


FIG. A1. (a) The Scorer parameter $l^2(z)$ for three simple cases of constant l for $z < 50$ m and $l = 0$ above [subcritical (red); supercritical (green); and critical (blue)] and $l^2(z) = 0.01 \exp(z/10$ m) (orange) chosen to approximate one of the curves in Fig. 8 and (b) confirmation of the criticality test for the three simple cases and the finding that the observed flow is supercritical (orange).

2016). The depth and strength of the upstream surface-based inversion layer are thus entirely determined by radiative cooling, and only the flow speed and basin size are allowed to vary. In a separate and more idealized study, we are increasing the parameter space to cover a wider range of flow regimes.

While the two-dimensional simulations can explain the formation of the observed downslope-windstorm-type flows at the Meteor Crater, they also represent a simplification of the flow over the inherently three-dimensional crater. Effects such as flow splitting around the crater and flow convergence over the upstream crater sidewall are completely neglected in the two-dimensional setup. In addition, we have deliberately ignored the crater rim to avoid upstream blocking effects in the two-dimensional simulations, which, however, may also affect the flow.

Acknowledgments. We thank George Bryan (NCAR) for his help with the model simulations and Sebastian Hoch (University of Utah) for preparing Fig. 1. The research was funded by NSF’s Physical and Dynamic Meteorology Division through Grant AGS-1160730. The contributions of the METCRAX II participants listed as coauthors and in the acknowledgment section of Lehner et al. (2016) in collecting and processing the field data are gratefully acknowledged. We also thank the anonymous reviewers for their comments and suggestions, which helped to improve the manuscript.

APPENDIX

Flow Criticality Test

The linear wave equation for steady waves, known as the Taylor–Goldstein equation, is

$$\frac{\partial^2 \psi}{\partial z^2} + [l^2(z) - k^2] \psi = 0, \quad (A1)$$

with boundary condition $\psi(0) = 0$; if $l^2 \rightarrow 0$ above some height, then $|\psi| < \infty$ is the condition at $z \rightarrow \infty$. To test the criticality for a given $l(z)$, one defines a test function governed by the equation:

$$\frac{\partial^2 \psi_c}{\partial z^2} + l^2(z) \psi_c = 0. \quad (A2)$$

The test function is integrated from $z = 0$ upward with an arbitrarily specified value of $\partial \psi / \partial z$ at $z = 0$; if there is a zero crossing, the flow is subcritical, for in this case a finite eigenvalue k can be found in (A1), which produces a slower oscillation of ψ (with respect to ψ_c) and thus allows the satisfaction of the upper boundary condition, which in turn implies a standing wave is possible.

An example of how this works is shown in Fig. A1 for the case of a finite-depth layer $z_N = 50$ m with three settings of N/U such that Nz_N/U is greater than, less than, or equal to $\pi/2$ [subcritical, supercritical, or critical conditions, respectively (see Baines 1995, p. 176)] and

$N/U = 0$ above $z = z_N$. The red, green, and blue curves in Figs. A1a and A1b correspond, respectively, to the theoretically predicted cases of subcritical, supercritical, and critical cases and show that the simple procedure works.

The orange line in Fig. A1 is the profile $l^2(z) = l_s^2 e^{-z/\delta}$, where $l_s^2 = 0.01 \text{ m}^{-2}$ and $\delta = 10 \text{ m}$ are chosen to model one of the observed profiles shown in Fig. 8. The criticality test shows that this flow is supercritical, and hence lee waves are not expected to form. With the latter profile for $l(z)$, one can obtain the analytical solution to (A2):

$$\psi_c(z) = c_1 J_0[2l_s \delta e^{-(z/2\delta)}] + c_2 Y_0[2l_s \delta e^{-(z/2\delta)}], \quad (\text{A3})$$

where J_0 and Y_0 are Bessel functions of the first and second kind, respectively. To find the critical condition, we observe that in the limit, as $z \rightarrow \infty$, the second term also goes to infinity; this corresponds to either sub or supercritical conditions, as we have seen in the simple example of Fig. A1. The exactly critical case thus requires $c_2 = 0$. Thus, at $z = 0$, $\psi_c(0) = c_1 J_0(2l_s \delta) = 0$, and therefore the criticality condition is

$$l_s^2 = \frac{\gamma_{0,1}^2}{4\delta^2}, \quad (\text{A4})$$

where $\gamma_{0,1} \simeq 2.404$ is the first zero of J_0 . Equation (A4) is the analogous condition to the Scorer condition (5); the condition for lee waves is therefore

$$l_s \delta > 1.2. \quad (\text{A5})$$

REFERENCES

- Adler, B., C. D. Whiteman, S. W. Hoch, M. Lehner, and N. Kalthoff, 2012: Warm-air intrusions in Arizona's Meteor Crater. *J. Appl. Meteor. Climatol.*, **51**, 1010–1025, doi:10.1175/JAMC-D-11-0158.1.
- Arriitt, R. W., and R. A. Pielke, 1986: Interactions of nocturnal slope flows with ambient winds. *Bound.-Layer Meteor.*, **37**, 183–195, doi:10.1007/BF00122763.
- Axelsen, S. L., and H. van Dop, 2009a: Large-eddy simulation of katabatic winds. Part 1: Comparison with observations. *Acta Geophys.*, **57**, 803–836, doi:10.2478/s11600-009-0041-6.
- , and —, 2009b: Large-eddy simulation of katabatic winds. Part 2: Sensitivity study and comparison with analytical models. *Acta Geophys.*, **57**, 837–856, doi:10.2478/s11600-009-0042-5.
- Baines, P. G., 1995: *Topographic Effects in Stratified Flow*. Cambridge University Press, 482 pp.
- Bechtold, P., M. Köhler, T. Jung, F. Doblas-Reyes, M. Leutbecher, M. J. Rodwell, F. Vitart, and G. Balsamo, 2008: Advances in simulating atmospheric variability with the ECMWF model: From synoptic to decadal time-scales. *Quart. J. Roy. Meteor. Soc.*, **134**, 1337–1351, doi:10.1002/qj.289.
- Benjamin, T. B., 1962: Theory of the vortex breakdown phenomenon. *J. Fluid Mech.*, **14**, 593–629, doi:10.1017/S0022112062001482.
- Blackadar, A. K., 1962: The vertical distribution of wind and turbulent exchange in a neutral atmosphere. *J. Geophys. Res.*, **67**, 3095–3102, doi:10.1029/JZ067i008p03095.
- Brown, A. R., R. J. Beare, J. M. Edwards, A. P. Lock, S. J. Keogh, S. F. Milton, and D. N. Walters, 2008: Upgrades to the boundary-layer scheme in the Met Office numerical weather prediction model. *Bound.-Layer Meteor.*, **128**, 117–132, doi:10.1007/s10546-008-9275-0.
- Bryan, G. H., and J. M. Fritsch, 2002: A benchmark simulation for moist nonhydrostatic numerical models. *Mon. Wea. Rev.*, **130**, 2917–2928, doi:10.1175/1520-0493(2002)130<2917:ABSFMN>2.0.CO;2.
- Chou, M.-D., and M. J. Suarez, 1994: An efficient thermal infrared radiation parameterization for use in general circulation models. NASA Tech. Memo. TM-104606, 85 pp.
- Cotton, W. R., and Coauthors, 2003: RAMS 2001: Current status and future directions. *Meteor. Atmos. Phys.*, **82**, 5–29, doi:10.1007/s00703-001-0584-9.
- Cuxart, J., and M. A. Jiménez, 2007: Mixing processes in a nocturnal low-level jet: An LES study. *J. Atmos. Sci.*, **64**, 1666–1679, doi:10.1175/JAS3903.1.
- , and Coauthors, 2006: Single-column model intercomparison for a stably stratified atmospheric boundary layer. *Bound.-Layer Meteor.*, **118**, 273–303, doi:10.1007/s10546-005-3780-1.
- Deardorff, J. W., 1980: Stratocumulus-capped mixed layers derived from a three-dimensional model. *Bound.-Layer Meteor.*, **18**, 495–527, doi:10.1007/BF00119502.
- Denby, B., 1999: Second-order modelling of turbulence in katabatic flows. *Bound.-Layer Meteor.*, **92**, 65–98, doi:10.1023/A:1001796906927.
- Doran, J. C., J. D. Fast, and J. Horel, 2002: The VTMX 2000 campaign. *Bull. Amer. Meteor. Soc.*, **83**, 537–551, doi:10.1175/1520-0477(2002)083<0537:TVC>2.3.CO;2.
- Doyle, J. D., and D. R. Durran, 2002: The dynamics of mountain-wave-induced rotors. *J. Atmos. Sci.*, **59**, 186–201, doi:10.1175/1520-0469(2002)059<0186:TDOMWI>2.0.CO;2.
- , and —, 2007: Rotor and subrotor dynamics in the lee of three-dimensional terrain. *J. Atmos. Sci.*, **64**, 4202–4221, doi:10.1175/2007JAS2352.1.
- Durran, D. R., 2003a: Downslope winds. *Encyclopedia of Atmospheric Sciences*, J. R. Holton, Ed., Elsevier Science Ltd., 644–650.
- , 2003b: Lee waves and mountain waves. *Encyclopedia of Atmospheric Sciences*, J. R. Holton, Ed., Elsevier Science Ltd., 1161–1169.
- , and J. B. Klemp, 1987: Another look at downslope winds. Part II: Nonlinear amplification beneath wave-overturning layers. *J. Atmos. Sci.*, **44**, 3402–3412, doi:10.1175/1520-0469(1987)044<3402:ALADWP>2.0.CO;2.
- Fedorovich, E., and A. Shapiro, 2009: Structure of numerically simulated katabatic and anabatic flows along steep slopes. *Acta Geophys.*, **57**, 981–1010, doi:10.2478/s11600-009-0027-4.
- Fritts, D. C., D. Goldstein, and T. Lund, 2010: High-resolution numerical studies of stable boundary layer flows in a closed basin: Evolution of steady and oscillatory flows in an axisymmetric Arizona Meteor Crater. *J. Geophys. Res.*, **115**, D18109, doi:10.1029/2009JD013359.
- Grell, G. A., J. Dudhia, and D. R. Stauffer, 1995: A description of the fifth-generation Penn State/NCAR Mesoscale Model (MM5). NCAR Tech. Note NCAR/TN-398 + STR, 122 pp., doi:10.5065/D60Z716B.
- Grisogono, B., and D. Belušić, 2009: A review of recent advances in understanding the meso- and microscale properties

- of the severe Bora wind. *Tellus*, **61A**, 1–16, doi:10.1111/j.1600-0870.2008.00369.x.
- , and S. L. Axelsen, 2012: A note on the pure katabatic wind maximum over gentle slopes. *Bound.-Layer Meteor.*, **145**, 527–538, doi:10.1007/s10546-012-9746-1.
- Grubišić, V., and B. J. Billings, 2007: The intense lee-wave rotor event of Sierra Rotors IOP 8. *J. Atmos. Sci.*, **64**, 4178–4201, doi:10.1175/2006JAS2008.1.
- , and I. Stiperski, 2009: Lee-wave resonances over double bell-shaped obstacles. *J. Atmos. Sci.*, **66**, 1205–1228, doi:10.1175/2008JAS2885.1.
- Haiden, T., 2003: Prediction of jet speed and height in katabatic flow. *Extended Abstracts, EGS-AGU-EUG Joint Assembly*, Nice, France, EGS, AGU, and EUG, 8479.
- , and C. D. Whiteman, 2005: Katabatic flow mechanisms on a low-angle slope. *J. Appl. Meteor.*, **44**, 113–126, doi:10.1175/JAM-2182.1.
- , —, S. W. Hoch, and M. Lehner, 2011: A mass flux model of nocturnal cold-air intrusions into a closed basin. *J. Appl. Meteor. Climatol.*, **50**, 933–943, doi:10.1175/2010JAMC2540.1.
- Holden, J. J., S. H. Derbyshire, and S. E. Belcher, 2000: Tethered balloon observations of the nocturnal stable boundary layer in a valley. *Bound.-Layer Meteor.*, **97**, 1–24, doi:10.1023/A:1002628924673.
- Horst, T. W., and J. C. Doran, 1988: The turbulence structure of nocturnal slope flow. *J. Atmos. Sci.*, **45**, 605–616, doi:10.1175/1520-0469(1988)045<0605:TTSONS>2.0.CO;2.
- Jackson, P. L., G. Mayr, and S. Vosper, 2012: Dynamically-driven winds. *Mountain Weather Research and Forecasting*, F. K. Chow, S. F. J. DeWekker, and B. Snyder, Eds., Springer, 121–218, doi:10.1007/978-94-007-4098-3_3.
- Jiang, Q., J. D. Doyle, and R. B. Smith, 2006: Interaction between trapped waves and boundary layers. *J. Atmos. Sci.*, **63**, 617–633, doi:10.1175/JAS3640.1.
- Katurji, M., S. Zhong, M. Kiefer, and P. Zawar-Reza, 2013: Numerical simulations of turbulent flow within and in the wake of a small basin. *J. Geophys. Res. Atmos.*, **118**, 6052–6063, doi:10.1002/jgrd.50519.
- Kiefer, M. T., and S. Zhong, 2011: An idealized modeling study of nocturnal cooling processes inside a small enclosed basin. *J. Geophys. Res.*, **116**, D20127, doi:10.1029/2011JD016119.
- Kimura, F., and P. Manins, 1988: Blocking in periodic valleys. *Bound.-Layer Meteor.*, **44**, 137–169, doi:10.1007/BF00117296.
- Lareau, N. P., and J. D. Horel, 2015: Turbulent erosion of persistent cold-air pools: Numerical simulations. *J. Atmos. Sci.*, **72**, 1409–1427, doi:10.1175/JAS-D-14-0173.1.
- Lawson, J., and J. Horel, 2015: Analysis of the 1 December 2011 Wasatch downslope windstorm. *Wea. Forecasting*, **30**, 115–135, doi:10.1175/WAF-D-13-00120.1.
- Lehner, M., and Coauthors, 2016: The METCRAX II field experiment: A study of downslope windstorm-type flows in Arizona's Meteor Crater. *Bull. Amer. Meteor. Soc.*, **97**, 217–235, doi:10.1175/BAMS-D-14-00238.1.
- LeMone, M. A., K. Ikeda, R. L. Grossmann, and M. W. Rotach, 2003: Horizontal variability of 2-m temperature at night during CASES-97. *J. Atmos. Sci.*, **60**, 2431–2449, doi:10.1175/1520-0469(2003)060<2431:HVOMTA>2.0.CO;2.
- Lilly, D. K., 1978: A severe downslope windstorm and aircraft turbulence event induced by a mountain wave. *J. Atmos. Sci.*, **35**, 59–77, doi:10.1175/1520-0469(1978)035<0059:ASDWAA>2.0.CO;2.
- Lin, Y.-L., and T.-A. Wang, 1996: Flow regimes and transient dynamics of two-dimensional stratified flow over an isolated mountain ridge. *J. Atmos. Sci.*, **53**, 139–158, doi:10.1175/1520-0469(1996)053<0139:FRATDO>2.0.CO;2.
- Lock, A., 2011: Stable boundary layer modelling at the Met Office. *Proc. ECMWF GABLS Workshop on Diurnal Cycles and the Stable Boundary Layer*, Reading, United Kingdom, ECMWF, 137–148.
- Louis, J.-F., 1979: A parametric model of vertical eddy fluxes in the atmosphere. *Bound.-Layer Meteor.*, **17**, 187–202, doi:10.1007/BF00117978.
- , M. Tiedtke, and J. F. Geleyn, 1982: A short history of the operational PBL-parameterization at ECMWF. *Proc. Workshop on Planetary Boundary Layer Parameterization*, Reading, United Kingdom, ECMWF, 59–79.
- Mason, P. J., and A. R. Brown, 1999: On subgrid models and filter operations in large eddy simulations. *J. Atmos. Sci.*, **56**, 2101–2114, doi:10.1175/1520-0469(1999)056<2101:OSMAFO>2.0.CO;2.
- Mauritsen, T., 2011: Advancing closures for stably stratified turbulence in global atmospheric models. *Proc. ECMWF GABLS Workshop on Diurnal Cycles and the Stable Boundary Layer*, Reading, United Kingdom, ECMWF, 63–74.
- Mayr, G. J., and L. Armi, 2010: The influence of downstream diurnal heating on the descent of flow across the Sierras. *J. Appl. Meteor. Climatol.*, **49**, 1906–1912, doi:10.1175/2010JAMC2516.1.
- McCabe, A., and A. R. Brown, 2007: The role of surface heterogeneity in modelling the stable boundary layer. *Bound.-Layer Meteor.*, **122**, 517–534, doi:10.1007/s10546-006-9119-8.
- Mellor, G. L., and T. Yamada, 1982: Development of a turbulence closure model for geophysical fluid problems. *Rev. Geophys. Space Phys.*, **20**, 851–875, doi:10.1029/RG020i004p00851.
- Mobbs, S. D., and Coauthors, 2005: Observations of downslope winds and rotors in the Falkland Islands. *Quart. J. Roy. Meteor. Soc.*, **131**, 329–351, doi:10.1256/qj.04.51.
- Rafkin, S. C. R., R. M. Haberle, and T. I. Michaels, 2001: The Mars Regional Atmospheric Modeling System: Model description and selected simulations. *Icarus*, **151**, 228–256, doi:10.1006/icar.2001.6605.
- Richner, H., and P. Hächler, 2012: Understanding and forecasting Alpine foehn. *Mountain Weather Research and Forecasting*, F. K. Chow, S. F. J. DeWekker, and B. Snyder, Eds., Springer, 219–260, doi:10.1007/978-94-007-4098-3_4.
- Scorer, R. S., 1949: Theory of waves in the lee of mountains. *Quart. J. Roy. Meteor. Soc.*, **75**, 41–56, doi:10.1002/qj.49707532308.
- Seluchi, M., F. A. Norte, P. Satyamurty, and S. C. Chou, 2003: Analysis of three situations of the foehn effect over the Andes (zonda wind) using the Eta-CPTEC regional model. *Wea. Forecasting*, **18**, 481–501, doi:10.1175/1520-0434(2003)18<481:AOTSOT>2.0.CO;2.
- Sheridan, P. F., and S. B. Vosper, 2006: A flow regime diagram for forecasting lee waves, rotors and downslope winds. *Meteor. Appl.*, **13**, 179–195, doi:10.1017/S1350482706002088.
- , —, and A. R. Brown, 2014: Characteristics of cold pools observed in narrow valleys and dependence on external conditions. *Quart. J. Roy. Meteor. Soc.*, **140**, 715–728, doi:10.1002/qj.2159.
- Skamarock, W. C., and Coauthors, 2008: A description of the Advanced Research WRF version 3. NCAR Tech. Note NCAR/TN-475, 113 pp., doi:10.5065/D68S4MVH.
- Skyllingstad, E. D., 2003: Large-eddy simulation of katabatic flows. *Bound.-Layer Meteor.*, **106**, 217–243, doi:10.1023/A:1021142828676.
- Smith, C. M., and E. D. Skyllingstad, 2005: Numerical simulation of katabatic flow with changing slope angle. *Mon. Wea. Rev.*, **133**, 3065–3080, doi:10.1175/MWR2982.1.

- , and F. Porté-Agel, 2014: An intercomparison of subgrid models for large-eddy simulation of katabatic flows. *Quart. J. Roy. Meteor. Soc.*, **140**, 1294–1303, doi:10.1002/qj.2212.
- Smith, R. B., 1985: On severe downslope winds. *J. Atmos. Sci.*, **42**, 2597–2603, doi:10.1175/1520-0469(1985)042<2597:OSDW>2.0.CO;2.
- Smith, S. A., A. R. Brown, S. B. Vosper, P. A. Murkin, and A. T. Veal, 2010: Observations and simulations of cold air pooling in valleys. *Bound.-Layer Meteor.*, **134**, 85–108, doi:10.1007/s10546-009-9436-9.
- Soontjens, N., M. Stastna, and M. L. Waite, 2013: Numerical simulations of waves over large crater topography in the atmosphere. *J. Atmos. Sci.*, **70**, 1216–1232, doi:10.1175/JAS-D-12-0221.1.
- Tao, W.-K., S. Lang, J. Simpson, C.-H. Sui, B. Ferrier, and M.-D. Chou, 1996: Mechanism of cloud-radiation interaction in the tropics and midlatitude. *J. Atmos. Sci.*, **53**, 2624–2651, doi:10.1175/1520-0469(1996)053<2624:MOCRII>2.0.CO;2.
- Viterbo, P., A. Beljaars, J.-F. Mahfouf, and J. Teixeira, 1999: The representation of soil moisture freezing and its impact on the stable boundary layer. *Quart. J. Roy. Meteor. Soc.*, **125**, 2401–2426, doi:10.1002/qj.49712555904.
- Vosper, S. B., 2004: Inversion effects on mountain lee waves. *Quart. J. Roy. Meteor. Soc.*, **130**, 1723–1748, doi:10.1256/qj.03.63.
- , and A. R. Brown, 2008: Numerical simulations of sheltering in valleys: The formation of nighttime cold-air pools. *Bound.-Layer Meteor.*, **127**, 429–448, doi:10.1007/s10546-008-9272-3.
- Whiteman, C. D., and S. Zhong, 2008: Downslope flows on a low-angle slope and their interactions with valley inversions. Part I: Observations. *J. Appl. Meteor. Climatol.*, **47**, 2023–2038, doi:10.1175/2007JAMC1669.1.
- , S. W. Hoch, M. Lehner, and T. Haiden, 2010: Nocturnal cold air intrusions into a closed basin: Observational evidence and conceptual model. *J. Appl. Meteor. Climatol.*, **49**, 1894–1905, doi:10.1175/2010JAMC2470.1.
- Zardi, D., and C. D. Whiteman, 2012: Diurnal mountain wind systems. *Mountain Weather Research and Forecasting*, F. K. Chow, S. F. J. DeWekker, and B. Snyder, Eds., Springer, 35–119, doi:10.1007/978-94-007-4098-3_2.
- Zhong, S., and C. D. Whiteman, 2008: Downslope flows on a low-angle slope and their interactions with valley inversions. Part II: Numerical modeling. *J. Appl. Meteor. Climatol.*, **47**, 2039–2057, doi:10.1175/2007JAMC1670.1.
- , and F. K. Chow, 2012: Meso- and fine-scale modeling over complex terrain: Parameterizations and applications. *Mountain Weather Research and Forecasting*, F. K. Chow, S. F. J. DeWekker, and B. Snyder, Eds., Springer, 591–653, doi:10.1007/978-94-007-4098-3_10.
- Zilitinkevich, S. S., T. Elperin, N. Kleeorin, and I. Rogachevskii, 2007: Energy- and flux-budget (EFB) turbulence closure model for stably stratified flows. Part I: Steady-state, homogeneous regimes. *Bound.-Layer Meteor.*, **125**, 167–191, doi:10.1007/s10546-007-9189-2.
- , —, —, —, I. Esau, T. Mauritsen, and M. W. Miles, 2008: Turbulence energetics in stably stratified geophysical flows: Strong and weak mixing regimes. *Quart. J. Roy. Meteor. Soc.*, **134**, 793–799, doi:10.1002/qj.264.
- , —, —, V. L'vov, and I. Rogachevskii, 2009: Energy- and flux-budget turbulence closure model for stably stratified flows. Part II: The role of internal gravity waves. *Bound.-Layer Meteor.*, **133**, 139–164, doi:10.1007/s10546-009-9424-0.
- , —, —, I. Rogachevskii, and I. Esau, 2013: A hierarchy of energy- and flux-budget (EFB) turbulence closure models for stably-stratified geophysical flows. *Bound.-Layer Meteor.*, **146**, 341–373, doi:10.1007/s10546-012-9768-8.